TAMPERE UNIVERSITY OF TECHNOLOGY

MIKKO NÄRHI

TOWARDS COMPLETE CHARACTERIZATION OF SUPER-CONTINUUM COHERENCE

Master of Science thesis

Examiner: Prof. Goëry Genty
Examiner and topic approved in the
Faculty of Natural Sciences Council
meeting on 04.12.2013

TIIVISTELMÄ

TAMPEREEN TEKNILLINEN YLIOPISTO
Teknis-luonnontieteellinen koulutusohjelma
MIKKO NÄRHI: Kohti täydellistä superkontinuumin koherenssin määritystä
Diplomityö, 69 sivua
Tammikuu 2014
Pääaine: Teknillinen fysiikka
Tarkastajat: Prof. Goëry Genty
Avainsanat: superkontinuumi, koherenssi, toisen asteen koherenssi

Työssä esitellään ja toteutetaan ensimmäistä kertaa superkontinuumin toisen asteen koherenssiominaisuuksien kokeellinen määritys. Kokeellinen menetelmä perustuu toisen asteen koherenssifunktioiden jakamiseen likimääräisesti kahteen erilliseen osaan. Tämä approksimatiivinen jako koherenttiin ja kvasi-staattiseen (engl. quasi-stationary) osaan havaittiin vasta hiljattain numeeristen simulaatioiden yhteydessä. Diplomityön tarkoituksena on todentaa nämä numeeriset havainnot kokeellisesti.
Työssä käsitellään tulosten analysoimisen helpottamiseksi niitä fysikaalisia prosesseja sekä kokeellisia parametrejä, jotka vaikuttavat superkontinuumin koherenssiominaisuuksiin. Lisäksi teoriaosuudessa esitellään toisen asteen koherenssifunktiot, joita voidaan soveltaa superkontinuumin käyttäytymisen tutkimiseen optisissa mittajäjestelyissä. Erityistä huomiota kiinnitetään myös koejärjestelyiden tarkkaan kuvaamiseen ja mahdollisten ongelmien ratkaisuun, jotta koherenssifunktioiden kokeellinen määrittäminen onnistuu luotettavasti.
Kokeelliset tulokset esittelevät kolme erillistä tapausta: täysin koherentin, osittain koherentin sekä epäkoherentin superkontinuumin, jotka kaikki on luotu femtosekuntilaserin sekä erikoisvalmisteisten optisten kuitujen avulla säätämällä pulssien sisäänmenotehoa kuituun. Saatuja mittaustuloksia verrataan simuloituihin tuloksiin, joita varten on käytetty kokeita vastaavia parametrejä. Hyvä vastaavuus laskennallisten ja kokeellisten tulosten kanssa on havaittavissa, mikä vahvistaa numeerisesti havaitun likimääräisen jaottelun oikeanmukaisuutta ja luo pohjaa tuleville tutkimuksille alalla.

ABSTRACT

TAMPERE UNIVERSITY OF TECHNOLOGY
Master's Degree Programme in Science and Engineering
MIKKO NÄRHI: Towards complete characterization of Supercontinuum coherence
Master of Science Thesis, 69 pages
January 2014
Major: Advanced Engineering Physics
Examiner: Prof. Goëry Genty
Keywords: supercontinuum, coherence, second order coherence

Experimental characterization of supercontinuum second order coherence properties is performed for the first time. The experimental method is based on an approximation separating the supercontinuum second order coherence functions into coherent and quasi-stationary parts. The approximation was discovered recently in light of numerical studies and the objective of the work in the thesis is to verify these numerical results experimentally.

In the theory section the mathematical formulation of the coherence functions is given accompanied with discussion of the physical meaning of the functions. Furthermore the physical processes and experimental parameters affecting supercontinuum coherence properties are adressed to further understand the behavior of the results. The possibility for using approximations of the second order coherence functions for modeling supercontinuum behavior in optical systems is also considered. Finally emphasis is put also on describing the various experimental methods used to ensure reliable retrieval of the coherence functions.

Experiments are performed for three distinct cases: coherent, partially coherent and incoherent supercontinuum generated in a photonic crystal fiber by a Ti:Sapphire femtosecond laser with an adjustable peak power for the input pulse. Obtained results are compared to simulated results generated with parameters corresponding to the experiment. Good agreement between the experimental and numerical results is observed, further justifying the approximation made and laying groundwork for future studies made in the field.

PREFACE

This thesis was done in the Physics department of Tampere University of Technology in the Optics laboratory. Building of the experimental setup started in early 2013 and the actual measurements presented in the thesis were done in August 2013 followed by the numerical simulations and analysis in the autumn. A large thank you goes to Professor Goëry Genty for having such farsightedness in planning the steps from my early years in the laboratory to achieve the results presented today in the thesis. His help has been also invaluable in the writing process and numerical simulations done to complement the experimental results.
Special thanks go to Dr. Miro Erkintalo for being a great instructor for the first years and teaching the habits of the Optics laboratory, M.Sc. Mariusz Zdanowicz for helping out with experimental issues and M.Sc. Aku Antikainen providing great company academically as outside the university as a fellow student in the laboratory. I would also like to thank everyone else in the laboratory for the warm, supportive and scientifically free atmosphere.
Finally I want to express my gratitude to my parents Esko and Kaisu for supporting me in my studies and always emphasizing the importance of learning throughout ones life.

Mikko Närhi,
Tampere, 7.1.2014

CONTENTS

LIST OF SYMBOLS AND ABBREVIATIONS

Abbreviations

CM	Coherent mode representation, an approximation of CSD/MCF
cs	Coherent square, part of the CSD/MCF
CSD	Cross spectral density, two-dimensional measure of correlations, see MCF
CW	Continuous wave laser
EF	Elementary field representation, an approximation of CSD/MCF
FROG	Frequency-resolved optical gating, pulse characterization technique
FSSM	Fourier split-step method, used to solve the GNLSE numerically
FT	Fourier transform, a mathematical analysis method
FWHM	Full width at half-maximum, pulse duration measure
FWM	Four wave mixing, a nonlinear process
DMI	Delayed Michelson interferometer, an interferometric measurement scheme
GNLSE	Generalized nonlinear Schrödinger equation, a class of differential equations
GS	Gerchberg-Saxton algorithm, an algorithm used for phase retrieval
GVD	Group velocity dispersion, parameter describing fiber dispersion
HIO	Hybrid input-output algorithm, an algorithm used for phase retrieval
HWP	Half-wave plate, an optical component to control the direction of polarization
IFT	Inverse Fourier transform, see FT
MCF	Mutual coherence function, two-dimensional measure of temporal coherence properties
MI	Modulational instability, phase-matched four-wave mixing

OCT	Optical coherence tomography, a measurement technique
PCF	Photonic crystal fiber, special type of otpical fiber
qs	Quasi-stationary part, part of the CSD/MCF
SC	Supercontinuum
SHG	Second harmonic generation, a nonlinear process
SFG	Sum-frequency generation, a nonlinear process
SRS	Stimulated Raman scattering, a nonlinear process
SPM	Self phase modulation, a nonlinear process
TBP	Time-bandwidth product, a fundamental limitation for spectral and temporal widths
THG	Third harmonic generation, a nonlinear process
WLI	White light interferometry, a measurement technique
ZDW	Zero dispersion wavelength, an optical fiber characteristic
XFROG	Crosscorrelation Frequency-resolved optical gating, pulse characterization technique
XPM	Cross phase modulation, a nonlinear process

Symbols

β	Propagation constant
β_n	Dispersion coefficient of order n
ϵ_0	Vacuum permittivity
$\gamma(t_1, t_2)$	Normalized Mutual coherence function
γ_{NL}	Nonlinear coefficient of an optical fiber
$\Gamma(t_1, t_2)$	Mutual coherence function
Γ_R	Spontaneous Raman noise
λ	Wavelength

$\mu(\omega_1, \omega_2)$	Normalized cross spectral density
$\bar{\mu}$	Overall degree of spectral coherence
$\chi^{(n)}$	Susceptibility of order n
$\psi_{(n)}$	Coherent mode of order n
ω	Angular frequency in rad/s
ω_0	Center angular frequency in rad/s
$A(z,t)/A$	Electric field amplitude/envelope
A_C	Coherence area
A_{eff}	Effective mode area
c	Speed of light in vacuum
$E(t)$	Complex electric field in time domain
$\tilde{E}(\omega)$	Complex electric field in frequency domain
f	Natural frequency of oscillations
$g(t)$	Gate pulse used in a FROG measurement
D	Dispersion parameter
$g_{12}^{(1)}$	First order coherence function
$g(\Omega)$	Modulation instability gain
$I(t)$	Mean intensity
J_l	Bessel function of l:th kind
K_l	Modified Bessel function of l:th kind
L_C	Coherence length
N	Soliton order
$n/n(\omega)$	Refractive index
n_2	Nonlinear refractive index
n_C	Fiber core refractive index

n_{CL}	Fiber cladding refractive index
n_{eff}	Effective refractive index
p	Dipole moment
p_c	Weight function, coherent contribution
p_q	Weight function, quasi-stationary contribution
$p(t)$	Probe pulse under study in a FROG measurement
P	Material polarization
$P(t)$	Instantaneous power in a fiber
P_p	Laser pulse peak power
$R(T)$	Raman response function
$S(\omega)$	Mean spectrum
$S(\tau, \omega)$	Fequency resolved optical gating spectrogram function
t_C	Coherence time
T_0	Laser pulse duration parameter for a hyperbolic secant pulses
T_{FWHM}	Laser pulse duration, FWHM
$u(r, \omega)$	Electric field distribution in an optical fiber
$V(\tau/\omega)$	Visibility of fringes in time/frequency domain
$W(\omega_1, \omega_2)$	Cross spectral density

1. INTRODUCTION

Supercontinuum light sources have attracted a lot of interest in the past two decades. This has been mainly caused by the number of potential applications. Even though supercontinuum (SC) generation was discovered in bulk glass already in the 1970's by Alfano and Shapiro [1], it was not until advancements in 1990's in both passively mode-locked ultrashort (pulse durations of < 1 ps) laser sources [2; 3; 4] and optical fiber manufacturing techniques (photonic crystal fibers and microstructured tapered fibers)[5; 6] has made it possible to study this diverse physical process in detail. A significant amount of scientific effort has then been put into understanding the SC generation under various experimental conditions [7; 8; 9] and modeling it numerically [10; 11; 9].

As the attainability and understanding of the SC sources improved, the road was paved for applications. The broad spectral bandwidth of SC matched only by thermal light sources with the directionality and brightness of laser light received immediate interest from engineers & physicists and numerous measurement techniques were either improved or invented with the help of SC light [12; 13; 14; 15].

However, with some of the processes for SC generation being noise driven [16; 17; 18; 10], the shot-to-shot stability of these sources can vary vastly. For example in applications such as optical frequency combs one a very high stability (i.e. consecutive SC produced by the pump laser are identical) is required. For this applicational reason studies trying to characterize the mechanisms affecting the stability [19; 20] and quantizing it [21; 22].

Applicationwise the Dudley-Coen first order degree of coherence for SC [21] is straightforward to implement and yields shot-to-shot stability information sufficient for most applications. However, it does not describe correlations between different spectral components of the SC spectrum as it is a first order coherence measure. Thus for a better understanding of the noise effects and their influence in SC generation, a second order coherence theory approach for nonstationary light is required [23; 24]. Even though numerical simulations can reproduce experimental results to a good degree [25; 26; 10] and second order correlations between different frequencies can be studied numerically straightforwardly, experiments have yet to confirm the analytical and numerical observations.

Determining the second order coherence properties experimentally is not straight-

forward. A recent observation from numerical studies approximately separated the second order coherence functions into two distinctive contributions (coherent and stationary) [24]. This separation has opened a venue into experimental characterization [27]. The work done in this thesis presents the first experimental characterization of these second order correlations (both in time and spectral domains) for SC light utilizing the recent numerical findings.

The thesis starts by addressing SC generation mechanisms in optical fibers with emphasis on processes that may alter SC stability. An introduction into numerical modeling of SC generation in fibers is also given to support the simulations done in the thesis. After this a short chapter describing the general mathematical tools for analysing the stability (or coherence) properties is given followed by a more in-depth view on SC second order coherence properties in chapter four. In the final chapters the experimental methods are described and the results are presented and analyzed and compared to simulated results. Validity of the separation and measures to improve experimental results further are also discussed.

2. SUPERCONTINUUM GENERATION

Supercontinuum as a term was first used by Manassah et al. [28] in 1984. In short it can be described as a remarkable spectral broadening of the laser pulse spectrum due to various nonlinear processes. Spectral broadening of only 60 nm can be sometimes considered as SC, but spectral broadening spanning over one octave (i.e. the bandwidth spans from the lowest frequency ω to double of this frequency 2ω) are easily achieved in practice.

Supercontinuum generation is in general a complex physical process, arising from a mixture of nonlinear effects sometimes affecting each other. These various mechanisms are well understood and explained in detail in the review by Dudley *et al.* [10]. Numerical models based on the generalized nonlinear Schrödinger equation (GNLSE) are able to reproduce the experimental results to a good accuracy [25; 26]. Even though SC generation is also possible with continuous wave (CW) lasers, pulsed sources are often used for because they can provide higher peak power and allow for more efficient nonlinear effects. A pulsed source was also used in the study of this thesis. Thus from here on, unless otherwise mentioned, lasers are to be assumed to be pulsed. We next briefly review the most significant theoretical concepts of light propagation and nonlinear effects in fibers. After this the numerical methods of modeling for SC generation are described. The chapter ends with examples of SC applications.

2.1 Linear light propagation in optical fibers

The concept of guiding and trapping light in waveguides by total internal reflection was demonstrated already in the 19th century by trapping sunlight inside the stream of water pouring out from a barrel [29]. Even though the phenomenon was known for a long time, it was not until 1960's and 1970's that it started to draw significant attention. The reason for this was the pioneering work of Charles Kao in purely dielectric optical fibers with low losses and which combined with optical amplifiers have enabled all-optical communication systems [30; 31]. Of course a wide range of fiber-based applications have also been invented (e.g. fiber optic probes for biomedical science [32] or fiber lasers for welding [33]).

A schematic of an optical fiber with core diameter $2a$ is shown in figure 2.1. Total internal reflection effect requires the fiber core to have a higher refractive index than

the cladding (i.e. $n_C > n_{CL}$).

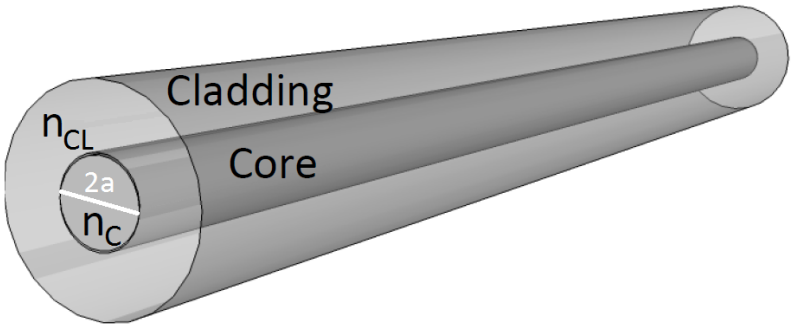

Figure 2.1: An optical fiber with core diameter $2a$.

After this the progress has been rapid and along with the simultaneous development of ultrashort pulsed lasers has lead to the fact that the modern information society could not be supported without these inventions. From a physicists point of view it has opened up new possibilities to study fundamental light-matter interactions over long distances in a more controllable manner.

Obviously the plethora of applications has lead to the fact that there exists plenty of theory describing light propagation in these fibers under various conditions (e.g. different modes in fibers, possible refractive index variation profiles, nonlinear phenomena). For SC generation the nonlinear effects are of most importance. But as we will devote one section for nonlinear effects only, let us first look at the most important concept of fiber optical thoery in the linear optics regime. This is the dispersion. For a more comprehensiver review on theory behind the light propagation in fibers, the reader is advised to see the book by Agrawal [31].

2.1.1 Dispersion

When introducing dispersion for the first time, an image of a prism separating white light into distinct colors of the rainbow is often shown. The reason behind the separation is the wavelength (or frequency) dependence of the refractive index, which is often referred as *material dispersion* in optics, as it is an inherent property of the material in question caused by the response of electrons to the incident light. In practice this is seen as different colors of light traveling at different velocities or taking different paths in the material. This causes the bending of light rays of different colors into different angles in a prism to preserve momentum.

When talking about guided light propagation in waveguides, the geometry of the waveguide can also affect the effective refractive index 'seen' by different wavelengths. This is caused by the fact that the solutions for the modes (i.e. electric field distributions) in the waveguide are also wavelength-dependent, causing shorter

wavelengths to be more confined in the core of the fiber. This is called *waveguide dispersion*. The electric field distributions $u(r, \theta, \omega)$ can be solved with the help of Maxwell's equations and posing a boundary condition that the tangential components of the magnetic and electric fields are continuous in the core-cladding interface. The solution in radial coordinates is given by [31]

$$u(r,\theta,\omega) = \begin{cases} J_l(\kappa r)\cos(l\theta), & r \leq a \quad \text{(core)} \\ K_l(\eta r)\cos(l\theta), & r > a \quad \text{(cladding)}, \end{cases} \tag{2.1}$$

where $\kappa = \sqrt{n_C^2 k_0^2 - \beta_m^2}$ and $\eta = \sqrt{\beta_m^2 - n_{CL}^2 k_0^2}$ are defined with the help of the core and cladding refractive indices n_C and n_{CL} respectively. J_l is the l:th order of Bessel function, K_l is the l:th order of modified Bessel function. β_m describes the frequency dependent propagation constant for the mode m and is usually solved numerically. It can also be defined as $\beta_m = \beta(\omega) = n(\omega)k_0$, where $n(\omega)$ is the frequency dependent refractive index and $k_0 = 2\pi/\lambda$ is the wave vector of the propagating light in vacuum. The total dispersion effects, resulting from the material dispersion and waveguide dispersion, are thus completely described with the help of $\beta(\omega)$.

Examples of the modes described above are illustrated in the figure 2.2.

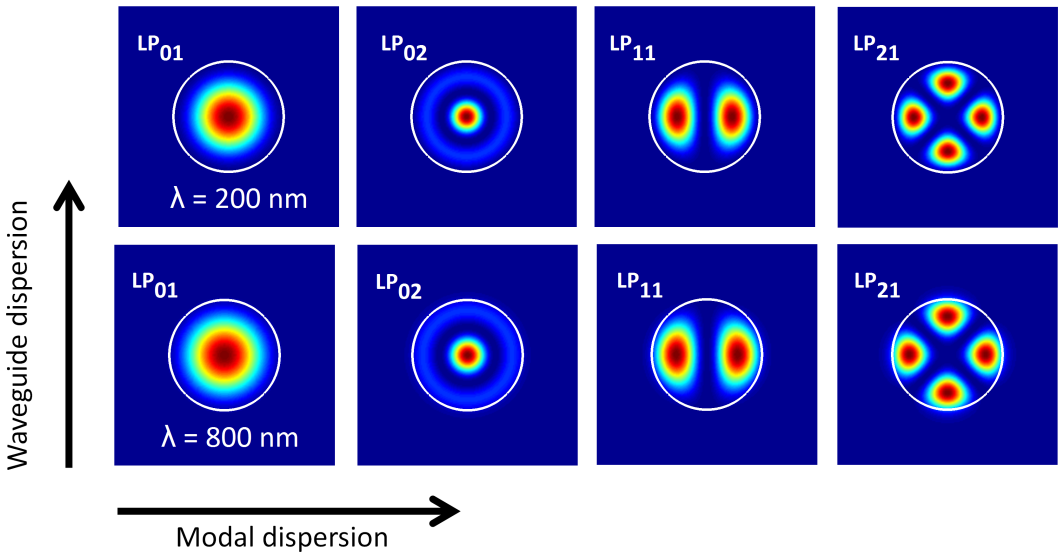

Figure 2.2: Some of the possible electric field distributions (LP_{lm} modes) in an optical fiber (white ring). The top row has been calculated with a laser wavelength of 200 nm and bottom row with 800 nm. Note the different mode size between these two which is most apparent in the LP_{21} mode. This is the waveguide dispersion.

The modes in the figure were calculated for fixed fiber parameters and simply varying the wavelength. Different transverse mode profiles may be allowed at a given wavelength. These are illustrated in the horizontal direction. The various LP_{lm}

modes also propagate with different velocities, this is referred as *modal dispersion*. [31]

If the core size of the fiber (white ring in the figure) is small enough, the higher order modes cannot exist anymore. A fiber that has small enough core and supports only the LP_{01} mode is called a *single-mode fiber*. The fiber used in the thesis is a single-mode fiber at all wavelengths and thus modal dispersion effects can be neglected. The condition for single-mode operation for fibers is given by the V-parameter defined as $V = 2\pi\frac{a}{\lambda}\sqrt{n_C^2 - n_{CL}^2}$. It follows from the properties of the Bessel functions of eq. 2.1 that a single-mode fiber is achieved when $V < 2.405$ [31].

The propagation constant $\beta(\omega)$ can often be approximated as a Taylor series around the center frequency ω_0 of the pulse propagating in the medium,

$$\beta(\omega) = \beta(\omega_0) + \beta_1(\omega - \omega_0) + \frac{1}{2}\beta_2(\omega - \omega_0)^2 + \frac{1}{6}\beta_3(\omega - \omega_0)^3 + ... \qquad (2.2)$$

Here $\beta_n = \frac{d^n\beta(\omega_0)}{d\omega^n}$. The β_1 parameter corresponds to the group delay of propagation in materials. It describes how fast different colors (frequencies) propagate in an optical fiber. For a laser pulse containing multiple frequencies this is the cause for pulse broadening in time since different colors travel at different speeds. The temporal broadening can be calculated with the help of the $\beta_2 = \frac{d^2\beta(\omega_0)}{d\omega^2}$, which is known as the group velocity dispersion (GVD) parameter. Higher order dispersion parameters can also cause pulse distortions, but are often negligible compared to the effects of the second order parameter [31].

Depending on the sign of β_2 dispersion is either classified as *normal* ($\beta_2 > 0$) or *anomalous* ($\beta_2 < 0$). Usually materials and fibers experience normal dispersion. This causes the longer wavelengths to travel faster. Consequently this leads to temporal broadening of the pulse and a distribution of different frequencies at different time-instants of the pulse (this is also referred as the pulse being down-chirped). In the case of anomalous dispersion the opposite occurs and short wavelengths are at the leading edge of the pulse (referred as up-chirp).

With advancements in fiber manufacturing technologies it has become possible to manufacture fibers with tailorable dispersion profiles and even with anomalous dispersion at visible wavelengths [34]. The latter one will be of importance when we discuss SC generation in more detail later. It is also noted, that dispersive effects are often unobservable unless a pulsed laser source with non-negligible bandwidth is used.

2.2 Nonlinear fiber optics

One of the two major technical steps mentioned above enabling SC generation has been the progress in mode-locked femtosecond regime lasers. First of these have been

demonstrated already in the 1980's (e.g. Rolland et al. [35]), however it was not until 1990's that the sources became more widespread and available [4]. Limited by the Fourier transform property for a time signal and its frequency-domain counterpart, the shorter the laser pulse is, the more spectral bandwidth it must have. This is known as the *time-bandwidth product* (TBP) [36]. For example the laser pulse durations used in this work were roughly $\approx$ 70 fs (full width at half-maximum, FWHM) and had a spectral bandwidth of $\approx$ 17 nm. This is quite different from the traditional idealistic image of a laser being purely monochromatic and emitting light continuously. A pulse for which this TBP is at minimum is called a *transform-limited pulse*.

As the pulse peak power is inversely proportional to the duration of the pulse, peak powers in the order of kilowatts are readily obtained in pulsed sources (even values close to petawatts have been obtained in laboratories [36]). This also means that the electric field amplitude within the pulse reaches values on the order of 10^{11} V/m. This value is considered as a threshold value when the optical electric field is comparable to the interatomic electric fields [37]. At this point the oscillating movement of electrons driven by the oscillating optical field cannot be described as regular harmonic oscillators but instead the movement becomes highly nonlinear. This is often described with the nonlinear polarizability of the material [37]. The branch of physics that studies the interactions of these strong electric fields within the material is known as *nonlinear optics*.

2.2.1 Material polarization and susceptibility

The usual approach to nonlinear optics is the susceptibility formalism, where light-matter interaction is modeled using susceptibility tensors of various ranks. Tensors are required to properly treat the vectorial nature of the electric field of light. Tensors are mathematical entities that transform vectors (and scalars) linearly similarly to scalar multiplication. Tensors can however in addition alter the direction of a vector. To introduce the tensor formalism, we consider first just a regular linear optics case.

When a static electric field $\mathbf{E}$ (vector quantities are bolded) is applied to a material, it moves the charges (usually electrons are the only ones capable of moving significantly) within the material. These charges in turn cause a dipole moment $\mathbf{p}$ oriented in the opposite direction with respect to the applied electric field. When we want to consider the total effect of n dipoles in the entire volume of the material, we need to know the number of dipole moments per unit volume of the material. This is the definition of the polarization $\mathbf{P}$ induced by the light field in the material (word material polarization is sometimes used to distinguish from light polarization)

$$\mathbf{P} = \frac{\text{total amount of dipole moments}}{\text{total volume}} = \frac{n\mathbf{p}}{V} = N\mathbf{p}, \tag{2.3}$$

where we have used the number density $N = n/V$ of the material. Intuitively it's clear that the polarization $\mathbf{P}$ depends on the electric field $\mathbf{E}$, however they need not to be parallel as one could anticipate. Because of the microscopic structure of the material, which might restrict the movement of electrons to certain directions, $\mathbf{P}$ might point to a different direction than the applied field. This is why the dependence needs to be formulated with a tensor. With the previous arguments in mind we write,

$$\mathbf{P}_{\text{LIN}} = \epsilon_0 \chi^{(1)} \cdot \mathbf{E}, \tag{2.4}$$

where ϵ_0 is the vacuum permittivity and the first order susceptibility $\chi^{(1)}$ (a rank 2 tensor) describes the material response to the field.

Next we consider the electric field to be rapidly oscillating with time, $\mathbf{E}(t)$ as is in fact in the case of light propagating in materials. As the electrons are very light, they can usually easily move along this rapidly alternating field. The energy absorbed from the light by the material in the form of moving electrons will again radiate light at the same frequency (an oscillating charge emits radiation) as that of the incoming electric field and thus light can propagate through (dielectric) materials unchanged in frequency. Possible changes through absorption can also be described with the imaginary part of the susceptibility $\chi^{(1)}$. The tensor nature of $\chi^{(1)}$ takes care of possible deflection of light entering a material (e.g. dispersion by prism). This is the linear optics perspective of light-matter interactions. For example, the refractive index $n(\omega)$ is often defined by the help of $\chi^{(1)}$ as follows [37],

$$n^2(\omega) = 1 + \chi^{(1)}. \tag{2.5}$$

The susceptibility can be thought of as a parameter describing the possibility of electrons to move in different directions in the material, thus affecting the speed and direction of propagation in the material via the refractive index. As mentioned above the susceptibility can vary depending on the incoming light direction as the atomic lattice of the material can restrict the electron movement. Furthermore, as the refractive index is frequency dependent, so is the susceptibility, and we should in reality write $\chi^{(1)} = \chi^{(1)}(\omega)$. This is sometimes left out to shorten notation, but should not be forgot. Also as mentioned, the light field can be thought of being absorbed and re-emitted in the material. Some of the energy might be permanently absorbed and this is described by the imaginary part of the susceptibility. Indeed, $\chi^{(1)}(\omega)$ is usually complex valued. [37]

2.2.2 Nonlinear polarization

If we increase the electric field amplitude above the atomic threshold value, the charges in the material start to get displaced more and their movement cannot be described anymore with a simple linear model as above. Thus we correct our model by adding higher order terms:

$$\begin{aligned}\mathbf{P} &= \epsilon_0 \left[\chi^{(1)} \cdot \mathbf{E} + \chi^{(2)} : \mathbf{E}^2 + \chi^{(3)} \vdots \mathbf{E}^3 + ...\right] \\ &= \epsilon_0 \chi^{(1)} \cdot \mathbf{E} \ + \epsilon_0 \left[\chi^{(2)} : \mathbf{E}^2 + \chi^{(3)} \vdots \mathbf{E}^3 + ...\right] \\ &= \mathbf{P}_{\mathrm{LIN}} + \mathbf{P}_{\mathrm{NL}},\end{aligned} \tag{2.6}$$

In the equation above, we have the regular linear polarization term accompanied with higher order terms of $\mathbf{E}$. The higher order terms contribute to the so called nonlinear polarization $\mathbf{P}_{\mathrm{NL}}$, which is the foundation for nonlinear optics. Because the values of the higher order susceptibilities $\chi^{(2)}$, $\chi^{(3)}$ etc. are much smaller compared to the first order susceptibility, the nonlinear terms require intense laser light to be observed [37]. Thus nonlinear optics are rarely observed in nature. The susceptibility model can explain only some of the phenomenon occuring in nonlinear optics. Nonlinear phenomena such as saturable absorbtion, stimulated scattering processes (e.g. Brillouin, Raman, Rayleigh) and acousto-optic effects cannot be described by the susceptibility formalism and require a different treatment [37]. The approach above provides nevertheless a useful and simple way to understand the background of nonlinear effects. For the rest of the discussion we will also neglect the vectorial and tensorial nature of the quantities in question. This simplifies the analysis without leaving any essential phenomenon undiscovered.

Before moving onto the nonlinear effects governing SC generation, we look at the the possibility of truncating the infinite series above for simplifying the analysis. Firstly, it can be shown that all even order susceptibilities vanish identically for centrosymmetric crystal structures in the dipole approximation [37]. This is significant, because the silica used in optical fibers is centrosymmetric. Secondly, the absolute values in the nonlinear susceptibility tensors $\chi^{(n)}$ become quickly smaller as n increases, meaning that very high field intensities would be required for these terms to contribute significantly. In normal optical materials these intensities would lead to ionization and material destruction, hence in most of the cases we can neglect fifth and higher order terms. This means that in terms of the susceptibility formalism, only the third order effects need to be considered. (In reality some second order effects can also be observed because of quadrupole and magnetic-dipole effects, but

these occur at such a low efficiency that they can be neglected in practice [29].)

2.2.3 Nonlinear processes in fibers

Next we will discuss the most important nonlinear effects in SC generation. But first we will define a useful quantity used also in describing some of the nonlinear effects later. The *nonlinear coefficient* (units W^{-1}/m) is a figure of merit for fibers describing the strength of nonlinear effects in the fiber and is given by [29]

$$\gamma_{\mathrm{NL}} = \frac{\omega_0 n_2(\omega_0)}{cA_{\mathrm{eff}}(\omega_0)}, \tag{2.7}$$

where $n_2(\omega_0)$ is the nonlinear refractive index at ω_0 (caused by the optical Kerr effect discussed below), c is the speed of light and A_{eff} is the electrical field mode effective area of the optical fiber in question (see fig. 2.2). Together with the pulse peak power P_0 they define the nonlinear length $L_{\mathrm{NL}} = 1/(\gamma_{\mathrm{NL}} P_0)$ which is a characteristic distance in which the nonlinear processes in fibers take place. [29]

Dispersive effects on the other hand occur at a distance $L_{\mathrm{D}} = T_0^2/|\beta_2|$, where $T_0 = T_{FWHM}/1.763$ is the pulse duration and β_2 is the GVD. When $L_{\mathrm{NL}} << L_{\mathrm{D}}$ nonlinear processes are expected to be significant in the fiber. In the other case, $L_{\mathrm{NL}} >> L_{\mathrm{D}}$, the pulse is expected to propagate in a linear manner. [29]

Optical Kerr effect

The Kerr effect in general refers to the variation of the refractive index of material by applying an external electric field. It is similar to the Pockels effect, but the Pockels effect depends linearly on the applied electric field whereas Kerr effect depends quadratically on the applied field [37]. This effect can be induced also by the electric field of a laser pulse traveling through a material without any external field. In this case it is called the *optical Kerr effect*. It is fairly straightforward to see how it arises with the help of the susceptibility formalism.

We apply a strong linearly polarized oscillating electric field $E(t) = Ae^{-i\omega t} + A^* e^{i\omega t}$, oscillating at the (angular) frequency $\omega = 2\pi f$ with an amplitude A, to a third order nonlinear material. Calculating the polarization induced by this field according to equation 2.6 (using a scalar approximation for simplicity) we get the following

$$
\begin{aligned}
P_{\text{total}} &= \epsilon_0[\overbrace{\chi^{(1)}E(t)}^{P_{\text{LIN}}} + \overbrace{\chi^{(3)}E^3(t)}^{P_{\text{NL}}}] \\
&= \epsilon_0 E(t)\left[\chi^{(1)} + \chi^{(3)}E^2(t)\right] \\
&= \epsilon_0 E(t)\left[\chi^{(1)} + \chi^{(3)}(A^2e^{-i2\omega t} + A^{*2}e^{i2\omega t} + 2|A|^2)\right] \\
&= \epsilon_0\chi^{(1)}(Ae^{-i\omega t} + c.c.) + \epsilon_0\chi^{(3)}\left[A^3e^{-i3\omega t} + A|A|^2e^{-i\omega t} + 2A|A|^2e^{-i\omega t} + c.c.\right] \\
&= \epsilon_0\chi^{(1)}(Ae^{-i\omega t} + c.c.) + \underbrace{\epsilon_0\chi^{(3)}(3A|A|^2e^{-i\omega t} + c.c.) + \epsilon_0\chi^{(3)}(A^3e^{-i3\omega t} + c.c.)}_{P_{\text{NL}}}.
\end{aligned}
\tag{2.8}
$$

This total polarization has terms oscillating at frequencies ω and 3ω. The terms oscillating at 3ω correspond to third harmonic generation (THG). These rapid charge oscillations radiate photons at a new frequency. Quantum mechanically this frequency tripling corresponds to three photons combining into one photon at a higher energy. Usually the THG radiation is not phase-matched (discussed later) and can be neglected.

We next turn our attention to the terms in the previous equation radiating light at the fundamental frequency ω. For clarity we neglect the c.c. terms as they contain no extra information. We write

$$
\begin{aligned}
P_{\text{total}}(\omega) &= \epsilon_0\chi^{(1)}Ae^{-i\omega t} + \epsilon_0\chi^{(3)}3A|A|^2e^{-i\omega t} \\
&= \epsilon_0 Ae^{-i\omega t}\left[\chi^{(1)} + 3\chi^{(3)}|A|^2\right] \\
&= \epsilon_0 Ae^{-i\omega t}\chi^{(1)}_{eff}
\end{aligned}
\tag{2.9}
$$

Here we have used the effective first order susceptibility $\chi^{(1)}_{eff} = \chi^{(1)} + 3\chi^{(3)}|A|^2$. Using equation 2.5 to calculate the effective refractive index $n_{eff} = n + \Delta n$ we get (assuming the variation Δn is small),

$$
\begin{aligned}
n^2_{eff} &= n^2 + 2n\Delta n + \Delta n^2 \\
&\approx n^2 + 2n\Delta n = 1 + \chi^{(1)}_{eff} = 1 + \chi^{(1)} + 3\chi^{(3)}|A|^2 \\
&\Rightarrow 2n\Delta n = 3\chi^{(3)}|A|^2 \quad \text{, because} \quad n^2 = 1 + \chi^{(1)} \\
&\Rightarrow \Delta n = \frac{3\chi^{(3)}|A|^2}{2n} = \frac{3\chi^{(3)}I}{4\epsilon_0 n^2 c} = n_2 I \\
&\Rightarrow n_{eff} = n + n_2 I
\end{aligned}
\tag{2.10}
$$

The last line follows from the fact that intensity depends on field amplitude as $I = 2\epsilon_0 nc|A|^2$. Thus we see that the induced nonlinear polarization causes an

intensity dependent refractive index, which is equivalent to the optical Kerr effect.

Self Phase Modulation

The intensity dependent refractive index means that a laser pulse can change the refractive index properties of the material while propagating. This results in an additional phase shift for the pulse in addition to the linear phase shift caused by propagation. This can be seen by considering an electric field propagating in the z-direction:

$$\begin{aligned} E(z,t) &= Ae^{-i(\omega t+kz)} + c.c. \\ &= Ae^{-i(\omega t+n_{eff}\frac{2\pi}{\lambda}z)} + c.c. \\ &= A\exp -i(\omega t + \underbrace{n\frac{2\pi}{\lambda}z}_{\text{LIN}} + \underbrace{n_2 I\frac{2\pi}{\lambda}z}_{\text{NL}}) + c.c. \end{aligned} \tag{2.11}$$

The last term in the exponent, $\varphi_{\text{NL}} = n_2 I\frac{2\pi}{\lambda}z$, corresponds to the additional phase shift. Because the source of this self-induced phase shift arises from the third order nonlinearity, it's often called the *nonlinear phase shift* or *self phase modulation* (SPM). In practice it causes chirping of the laser pulses, similar to that caused by normal dispersion [31]. This down-chirp means that longer wavelengths propagate faster within the pulse and are located on the leading edge. However, unlike dispersion, SPM itself does not broaden the laser pulse temporally but broadens the spectrum symmetrically [36]. Comparison between dispersive and SPM effects on a laser pulse propagating in a nonlinear fiber is shown in figure 2.3 below. This SPM spectral broadening is responsible for the SC generation when fs-timescale pulses are launched in a nonlinear fiber [10].

Cross phase modulation (XPM) is a phenomenon similar to SPM, but XPM refers to the case when one optical field affects the refractive index (and nonlinear phase shift) experienced by another co-propagating field with a different wavelength and/or state of polarization. The most significant difference with SPM is that the nonlinear phase shift induced by XPM will have a factor of two difference in magnitude compared to that induced by SPM. Also the spectral broadening caused by XPM can be asymmetric in the presence of higher-order dispersion. [29]

Solitons

In the anomalous dispersion regime SPM and XPM induced phase shifts can balance out with the dispersion effects (the chirp in figure 2.3 c is opposite to that of SPM induced nonlinear chirp in subfigure d) leading to the generation of *optical solitons*,

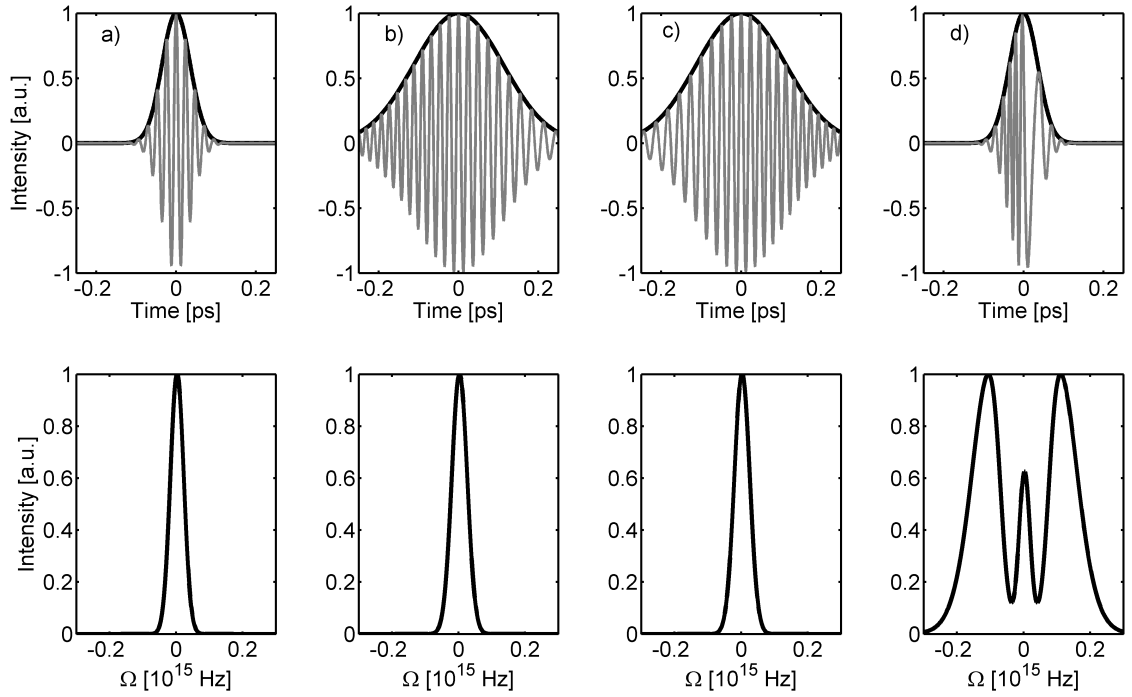

Figure 2.3: **Top row:** a) Transform-limited pulse, b) normal dispersion has broadened the pulse temporally and imposed a linear chirp (seen in the asymmetric oscillations), c) chirp caused by anomalous dispersion and d) pulse of subfigure a has experienced SPM induced nonlinear chirp. Note that the duration of the pulses is the same in a and d. The black line corresponds to pulse envelope and grey line to electric field amplitude. **Bottom row:** Corresponding spectra plotted versus offset from the pulse center frequency. Note the significant spectral broadening in the SPM case whereas dispersion causes no broadening.

waves that can propagate undistorted for long distances [38; 39].

The optical solitons in the anomalous dispersion regime are characterized by their *soliton order* $N = \sqrt{L_{\mathrm{D}}/L_{\mathrm{NL}}} = \sqrt{\gamma_{NL} P_0 T_0^2/|\beta_2|}$. Analytically the optical soliton of duration $T_0 = T_{FWHM}/1.763$ and peak power P_0 is of the form [10]

$$A(T, z = 0) = \sqrt{P_0}\mathrm{sech}\left(\frac{T}{T_0}\right). \tag{2.12}$$

Increasing the peak power also increases the soliton order N. The fundamental soliton ($N = 1$) propagates totally unchanged in a lightwave system, whereas the higher order solitons experience periodic change of shape during propagation. The temporal pulse shapes of fs-lasers are usually hyperbolic secants and can be considered as higher order solitons. Moreover, any reasonable pulse shape is expected to evolve into a (higher order) soliton [40]. Example of the evolution of a higher order ($N = 4$) soliton envelope is shown in both time and frequency in figure 2.4

Higher order solitons can be perturbed either by higher order dispersion or Raman scattering (discussed below) which can lead to the *soliton fission* process where

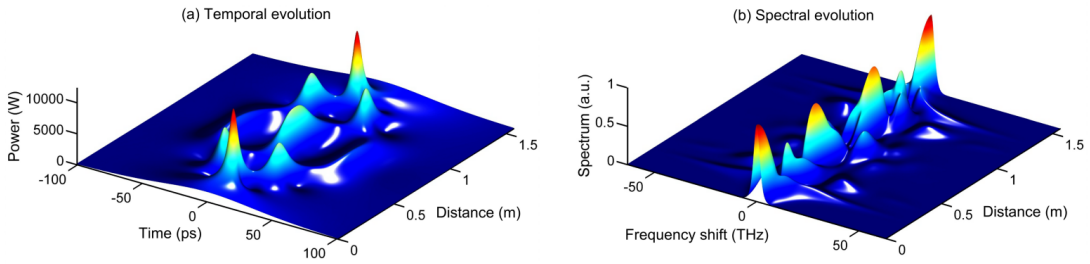

Figure 2.4: Evolution of a higher order soliton over one period in time and spectral domains. [41].

the input pulse (i.e. a higher order soliton) breaks up into individual fundamental solitons [29; 11]. These solitons can then shift their center frequency towards lower frequency via Raman scattering, which constitutes the main mechanism of SC towards the long wavelengths [10; 42].

There is often an associated *dispersive wave* with the ejected solitons. This dispersive wave is generated on the short wavelength side by the ejected soliton shedding a part of its energy as an optical Cherenkov radiation due to higher-order dispersion perturbations [43]. This extends the SC spectrum on the short wavelength side. Soliton fission plays a significant role in SC generation with pulses below 200 fs duration when the soliton order is relatively high.

Four Wave Mixing and Modulational Instability

Four wave mixing (FWM) refers to the interaction of four distinct frequencies $\omega_1, \omega_2, \omega_3$ and ω_4 via a third order nonlinearity. Physically it describes the annihilation and/or generation of four distinct photons. One can calculate the corresponding nonlinear polarization terms according to equation 2.6 as was done in equation 2.8. Because of four distinct fields interacting the result will have a large number of terms involving all the possible combinations of the four fields. However, most of the terms do not contribute significantly to the resulting field because of phase-mismatch

In order for a certain field at frequency ω_i to be amplified, net energy and momentum need to be conserved in the process. Energy conservation requires $\omega_4 = \pm\omega_1 \pm \omega_2 \pm \omega_3$ and momentum conservation requires $\Delta k = \beta_4 \pm \beta_3 \pm \beta_2 \pm \beta_1 = 0$, which is often referred as the *phase-matching* condition. Here $\beta_i = n_i\omega_i/c$ is the propagation constant at a given frequency. The $\pm$-signs can be chosen at will, representing all the possible frequency mixing combinations. [29]

The FWM process is called degenerate when two of the frequencies are the same e.g. $\omega_1 = \omega_2$. In this case the input pulse (pump at $\omega_0 = \omega_1 = \omega_2$) can amplify very weak sidebands located symmetrically about ω_0 by the FWM process. At the extreme, sidebands can even be generated from noise. The efficiency is often limited

by the phase-matching conditions, but even with partial phase-matching ($\Delta k \neq 0$) weak gain is allowed over a certain wavelength range for short propagation distances in fibers [29]. This kind of process is an important mechanism in SC generation with pulses of picosecond duration and longer.

SPM and XPM can contribute to phase-matching pf the FWM processes. In these cases the name *modulational instability*(MI) is also used for the process. MI actually describes the physical process in the time-domain, whereas FWM is the frequency-domain description. For the degenerate FWM/MI process phase-matched by SPM the gain can be shown to be given by [29]

$$g(\Omega) = |\beta_2 \Omega| \left(\frac{4\gamma_{NL} P_0}{|\beta_2|} - \Omega^2 \right)^{1/2}, \tag{2.13}$$

where $\Omega = \omega_0 - \omega$ describes the frequency offset from the pump center frequency, P_0 is the pump power, γ_{NL} is the nonlinear coefficient of the material/fiber and β_2 is the second order dispersion/GVD. The gain profile can be understood to be power-dependent because of the power dependence of SPM (as can be seen from eq. 2.11). The gain profile as given by equation 2.13 is illustrated in figure 2.5 versus the frequency detuning from the pump for various power values.

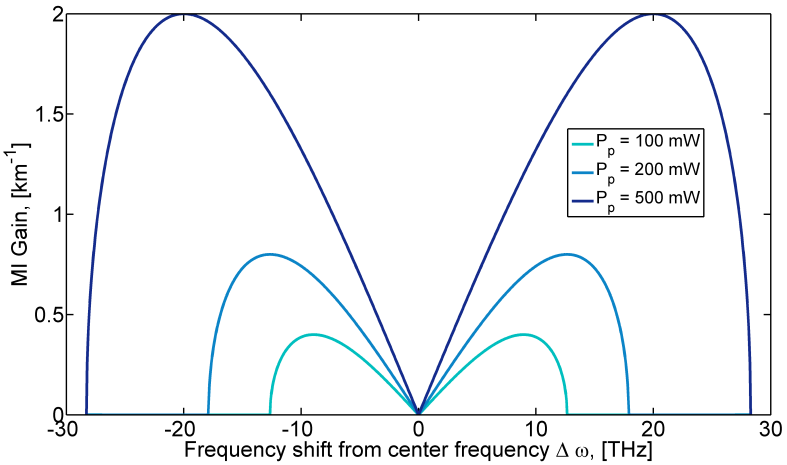

Figure 2.5: Modulation instability gain for various input powers. The frequency of maximum gain shifts away from the pump frequency as the peak power is increased.

Even though not apparent from the equation above, MI occurs in the anomalous dispersion ($\beta_2 < 0$) regime, even though it has also been shown that near the ZDW or for large frequency offsets the higher order dispersion parameters can allow for phase-matching even in the case of normal dispersion [44; 45].

The analysis above has considered CW light, but the results also apply for pulses

of ps durations and longer. FWM/MI is the dominant spectral broadening mechanism when generating SC with CW pumping or with picosecond or nanosecond pulses [46]. However, it has been shown that it also contributes to the spectral structure of SC generated with femtosecond pulses [47]. Because of the phase-matching condition is automatically satisfied in the anomalous dispersion regime, it can be readily understood why dispersion engineering had a significant impact on SC generation [10]. Finally we note that MI can have a significant impact on the SC coherence properties as it can amplify noise leading to a loss of coherence [48; 18].

Stimulated Raman Scattering

The Raman effect was discovered in 1928 by Indian physicist C.V. Raman [49]. Raman scattering refers to energy transfer by an inelastic collision from the vibrational energy states of the system (phonons) to photons. The nonlinear phenomena described previously are parametric (e.g. THG and FWM), meaning that the quantum state of the material stays unchanged throughout the light-matter interaction. In Raman scattering energy is clearly not conserved, and by it is thus referred to as a non-parametric process.

The collision causes the photon energy to be changed and thus frequency to be shifted. Shifting to both higher and lower frequencies is possible [37]. When the emitted photon has less energy (i.e. wavelength is longer than original and a red-shift is observed) the scattering is described as *Stokes scattering* and when the photon shifts to shorter wavelengths it is referred to *anti-Stokes scattering* or blue-shift. Of these two the Stokes scattering usually dominates, which follows from thermodynamical equilibrium arguments [37].

This spontaneous scattering process which occurs only for one photon in million scale [29] can also be stimulated when a weak amplitude wave co-propagates with an intense laser beam (compare to spontaneous emission of light vs. stimulated emission in laser crystals). In this case the term *stimulated Raman scattering* (SRS) is used. SRS can be associated with the imaginary part of the third order nonlinear susceptibility [37; 50]. Because of the amorphous nature of fused silica used in optical fibers it allows for energy transfer from vibrational states over a wide bandwidth [51]. The Raman gain parameter can be measured experimentally and is shown in figure 2.6.

SRS can generate new frequencies, leading to additional spectral broadening in SC. As with MI, also SRS can cause amplification of noise at the maximum of the gain spectrum [29; 16]. SRS is responsible for extending the spectrum further to longer wavelengths via the Stokes scattering process. SRS itself cannot lead to spectral broadening to short wavelengths as the gain spectrum is antisymmetric causing Anti-Stokes scattering to experience loss [37], however SRS coupled with

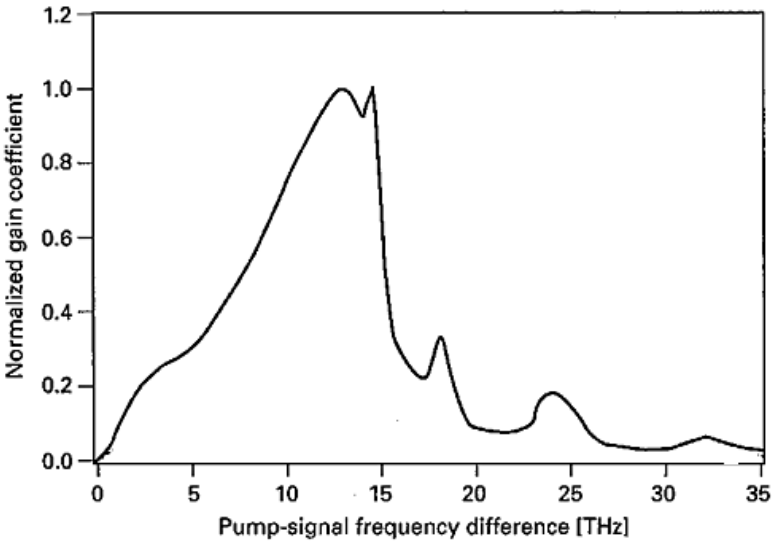

Figure 2.6: The normalized Raman gain spectrum for fused silica. After ref. [50].

FWM can also cause broadening to the blue end of spectrum [52; 53].

In the case of short pulses below picosecond durations the pulse bandwidth can be broader than the SRS gain bandwidth. In these cases the low frequencies of the pump pulse can amplify the high frequencies leading to a shift towards the longer wavelengths. If the pump pulse is located in the anomalous dispersion regime leading to solitonic behaviour the process is also referred to as the *soliton self-frequency shift*. As this effect is inversely proportional to the fourth power of pulse duration it can cause significant shift of the spectrum towards the longer wavelength side [42]. Furthermore, if the injected pulse is a higher order soliton the SRS will perturb the soliton and cause it to break down into fundamental solitons as discussed. These fundamental solitons can then experience an enhanced shift towards longer wavelengths extending the SC spectrum significantly [54; 29].

Lastly we note that Raman scattering is similar to Brillouin scattering. However Brillouin scattering occurs with decreased probability for short pulses and lower energy photons resulting in smaller frequency shifts. In addition the generated photons are counterpropagating with respect to the original light [29]. Thus Brillouin scattering can be completely neglected in the case of this thesis.

2.3 Modeling pulse propagation and SC generation

As can be understood from the discussion above, the nonlinear effects affecting the SC generation are often competing and coupled making it difficult to describe SC generation in a simple manner. Even though other mechanisms can be recognized as more significant under certain conditions, a general treatment of SC generation

usually requires taking all processes into account.

This multitude of competing and cooperating nonlinear processes and the stochastic nature caused by noise make the analysis difficult and thus the analysis is usually done by computational methods. Usually an ensemble of 100 simulations or more with random noise seed is implemented to investigate shot-to-shot stability. This has been shown to be a proficient method to reproduce experimental results to a good accuracy and has become the standard in modeling these effects. We will next discuss how this is done in practice to provide background on the numerical simulations of the thesis.

2.3.1 Nonlinear propagation equation

The nonlinear equation governing pulse propagation in nonlinear fiber optics is derived from Maxwell's equations and has various forms in both spectral and temporal domains [46]. The time-domain formulations of these nonlinear differential equations belong to the family of nonlinear Schrödinger equations, which have been studied extensively for example in the fields of superconductivity (the Ginzburg-Landau equation), ocean waves [55] and optics [56].

They have further been generalized to be suitable for modeling ultrashort pulse propagation in fibers [57]. The derivation of this Generalized nonlinear Schrödinger equation (GNLSE) is beyond the scope of the thesis, but the result will be represented here for overall consistency and general information. The following formulation follows the one used in reference [10], where the time T is represented in the co-moving frame of the fundamental laser pulse at group velocity β_1^{-1}. Here $A(z,t)$ is the complex envelope of the electric field.

$$\frac{\partial A}{\partial z} + \frac{\alpha}{2}A - \sum_{k\geq 2}\frac{i^{k+1}}{k!}\beta_k\frac{\partial^k A}{\partial T^k} = i\gamma_{NL}\left(1 + i\tau_{shock}\frac{\partial}{\partial T}\right) \times \left(A(z,T)\int_{-\infty}^{\infty} R(T')\left|A(z,T-T')\right|^2 dT' + i\Gamma_R(z,T)\right) \tag{2.14}$$

The left hand side of the equation represents linear propagation effects, α representing absorption and β_k being the dispersion coefficient from the abovementioned Taylor series expansion around the center wavelength ω_0. Usually up to 10 terms are used for the dispersion expansion to ensure accuracy. When working with PCF, short fiber lengths are used in experiments and absorption is no remarkable allowing us to set the α term to zero in simulations.

The right hand side corresponds to the nonlinear effects mentioned in the previous

subsection and their strength is characterized with the nonlinear coefficient γ_{NL} as discussed earlier.

The time derivative term associated with τ_{shock} models the dispersion of the nonlinearity. It is necessary to include it for the GNLSE to correctly model single cycle optical pulses of broad bandwidths, where the frequency dependence of the nonlinearity needs to be taken into account.

The multiplicative term on the second line of equation 2.14 takes SRS into account by the $R(T')$ term, which is the response function of the Raman scattering. It can be determined via the Kramers-Kronig relations and Fourier transform of the experimentally measured Raman gain parameter illustrated in figure 2.6 [50]. The final term Γ_R corresponds to spontaneous Raman noise, which is required to reproduce experimental results accurately (in some cases) as mentioned earlier.

2.3.2 Numerical modeling by the Fourier split-step method

Solving equation 2.14 is all but trivial, and general solutions do not exist as it is nonintegrable [29]. The Fourier split-step method (FSSM) is the standard technique used in nonlinear fiber optics to solve equation 2.14 , though other methods can be used. A comprehensive view on the method is given in the book by Agrawal [29]. Various modifications of the method do exist, but the underlying principle is the same in all of the methods.

The method separates the linear dispersive terms of the left hand side of eq. 2.14 from the nonlinear terms on the right. The idea behind this is that for propagation distances short enough in the fiber the normally simultaneous nonlinear and dispersive terms can be approximated to act independently. One first calculates the effect of dispersion over a short step of distance h, then calculates the effect of nonlinearity over the same propagation step. These two stages are then repeated sequentially until the end of the fiber is reached. A variation of the regular FSSM described here, is illustrated in figure 2.7.

The dispersive part is usually treated in the frequency-domain via a Fourier transform. Because of advanced FFT-algorithms this can be done in a fast manner. The convolution of the Raman response on the nonlinear side is also often calculated in the frequency-domain, as it transforms into a computationally fast multiplication. Rest of the nonlinear terms are usually integrated numerically by methods such as the second order Runge-Kutta algorithm. This method has shown to work well, when enough care is taken in choosing the propagation step size and the simulation grid parameters in time and frequency domains [10]. A single simulation realization solved by the FSSM is illustrated in figure 2.8.

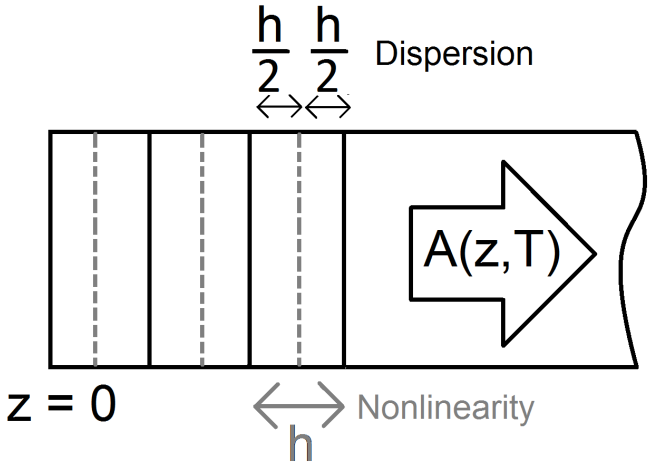

Figure 2.7: Symmetrized FSSM illustrated with a piece of optical fiber. Here the envelope $A(z,T)$ is first propagated with dispersion for half the step size $h/2$, then the nonlinearity is applied in the center of the step over the whole step length h, followed by dispersive propagation over $h/2$ to the end of the step. This method has proven to be more accurate compared to the original FSSM [29].

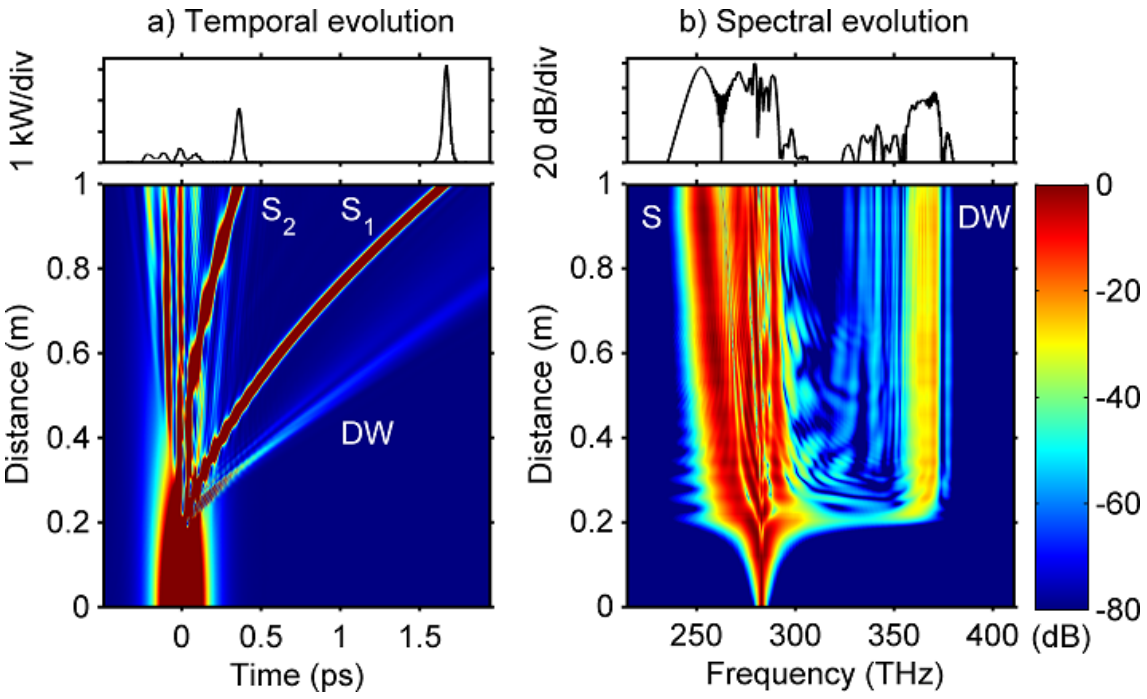

Figure 2.8: Simulation results for the evolution of a 200 fs pulse in an optical fiber. The two figures illustrate the a) time and b) spectral evolutions of the pulse at various propagation distances. Solitons ejected by the soliton fission process are highlighted in both domains by S and the corresponding dispersive wave by DW. Image taken from ref. [58].

2.4 Photonic Crystal Fibers

The other major step along pulsed laser sources enabling robust SC generation has been the advancements in optical fiber production techniques. Optical fibers in general work as a reliable platform for studying optical phenomenon because of the possibility of propagating the light without attenuation over long distances. In the context of nonlinear optics another factor is the confinement of light within the fiber. A small fiber core allows a high energy density of a focused pulse within the fiber enhancing the nonlinear effects. Even though SC generation has been demonstrated even in traditional fibers [59], photonic crystal fibers (PCF) provide a much tighter confinement in the narrow core and a tailorable dispersion profile by adjusting the hole lattice parameters surrounding the core.

It was not untill 1996 that the first PCF were succesfully produced by Knight et al [5]. An example of a PCF is illustrated in figure 2.9. In short, the structure has either a fused silica core or an air hole in the middle, where the light is confined. This core is then surrounded by a periodic lattice of airholes. Depending on whether the core is made of glass or is hollow the guiding effect of light is caused either by modified total internal reflection for a glass core [34] or the photonic band gap effect for hollow core fibers [60].

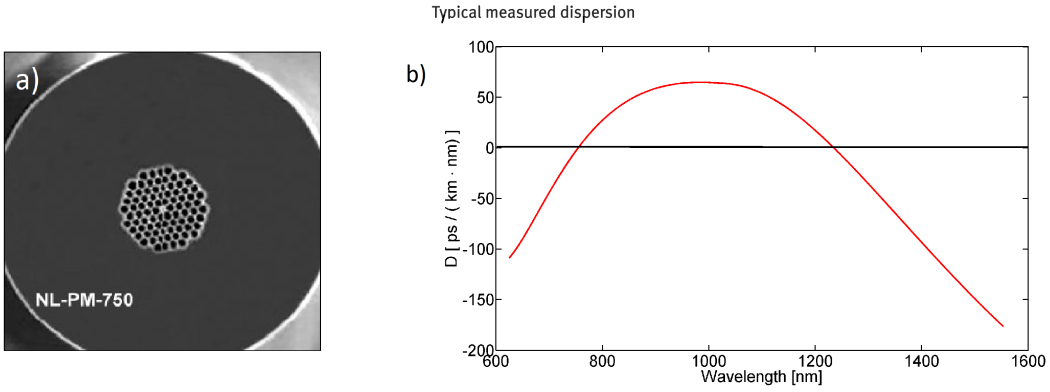

Figure 2.9: a) Scanning electron microscope image of the cross section of the fiber used in the experiments in this work. The fiber is polarization-maintaining. In b) the corresponding dispersion parameter D. The core diameter is $1.8\mu m \pm 0.3\mu m$ as reported by the manufacturer. The nonlinear coefficient is $\gamma_{\mathrm{NL}} = 95\ \mathrm{W}^{-1}/\mathrm{km}$ compared to standard fiber values of $1\ \mathrm{W}^{-1}/\mathrm{km}$. The fiber has two ZDWs at 750nm and 1235nm. Images are the courtesy of NKT Photonics.

Besides the large nonlinearity, another significant property of PCF , is the dispersion profile which can be engineered. More specifically the zero dispersion wavelength (ZDW) of the fiber can be shifted towards the wavelengths in the vicinity of the wavelengths emitted by ultrafast laser sources. The ZDW is defined as the wave-

length, where the fiber dispersion parameter $D = \frac{-2\pi c}{\lambda^2}\frac{d^2\beta}{d\omega^2}$ cancels. In principle laser pulses launched into the fiber at the ZDW will undergo minimal spreading in time by dispersion, though often higher order dispersion terms and nonlinearities become effective and cause distortion. ZDW engineering allows both normal and anomalous dispersion properties to be exploited, allowing different pump wavelength regimes to be explored for phase-matching FWM processes or trigger soliton fission processes responsible for SC generation mechanisms in fs and ps timescales respectively [10].

2.5 Applications

Even though creating laser rainbows in laboratory and studying the mechanisms is interesting *per se*, supercontinuum sources house a wide range of applications. Traditionally broadband white light sources have relied on blackbody radiation from thermal sources, leading to poor coherence (SC can have varying coherence properties) and directionality. Superluminescent diodes overcome the directionality problems at the cost of losing bandwidth, with the best ones spanning over 100 nm. Supercontinuum sources can overcome all of these problems with proper choices of fibers and pump laser sources.

Applications include spectroscopic studies where the broad bandwidth allows the use of the same source for simultaneous excitations of multiple compounds with high sensitivity [13]. Microscopy techniques can also benefit from the wide SC bandwidth. For example in confocal microscopy researchers have exploited the chromatic aberration often found as a hindrance as a depth probe in the study [61]. Other applications can be found in biomedical imaging of tissues such as Optical Coherence Tomography (OCT) used for finding defects in eyes [15], dynamic surface characterization by stroboscopic White Light Interferometry (WLI) [14] and accurate frequency combs for the most accurate frequency references available [62]. SC has also been used in broadband optical communication systems with wavelength-division multiplexing [63].

Even though applications exploiting SC are plenty, the requirements of SC properties depend highly on the application. Besides the broadband nature, the second order coherence (i.e. stability) of the SC affects strongly the performance of an application. For frequency combs, extremely stable sources are required, whereas the other extreme lie applications such as OCT and WLI requiring only a broad bandwidth. Thus determining and possibly manipulating the coherence properties of SC is desirable. In the next chapter we discuss the basic concepts behind coherence.

3. COHERENCE

Coherence is often introduced in the context of lasers and interference. For example Wikipedia defines coherence as "*an ideal property of waves that enables stationary interference*". Coherence can also be listed by any high-school student as a property of laser light. While both of these are true, they do not explain what coherence is. Interference can be observed even with incoherent light sources as e.g. in WLI. The concept of laser coherence becomes even more complex when consider pulsed (non-stationary) sources, where the optical intensity drops to zero between pulses. Obviously a more accurate and elaborate description is required.

The word correlation is perhaps the most useful word when talking about coherence. Indeed, nearly every instance of the word 'coherence' could be replaced with the word 'correlation' without any loss of information or generality. Correlation is defined in a dictionary as the "*mutual relation of two or more things, parts, etc.*" and this is essentially what coherence measures; the mutual relation between optical fields in two distinct space-time points. Obviously coherence and correlation can be found in other systems, but here we concentrate on the correlations between electric fields. This chapter attempts to clarify the concept and provide a mathematical background for studying coherence of electromagnetic waves. Most of the analysis here follows the book by Mandel and Wolf [64].

We take $E(\boldsymbol{r_i}, t_i)$ to represent the analytic (and thus complex) electric field at position $\boldsymbol{r_i}$ and time instant t_i. Its representation in the spectral domain will be noted with : $\tilde{E}(\boldsymbol{r_i}, \omega_i)$. We assume that the light is linearly polarized and thus we can neglect the vectorial nature of $E(\boldsymbol{r_i}, t_i)$ and take it to represent just the electric field component along a given Cartesian coordinate. It should be noted that this does not reduce the validity of the analysis, as extra dimensions can be easily implemented using the very same analysis. We further take the real valued (as an experimentally measurable quantity) instantaneous power $P(t)$ (often referred to instantaneous intensity outside fiber optics) to satisfy the condition

$$I(\mathbf{r}, t) = E^*(\mathbf{r}, t)E(\mathbf{r}, t). \tag{3.1}$$

3.1 Temporal and Spatial coherence

We start by looking at the traditional concepts of *temporal and spatial coherence*. Consider the situation depicted in figure 3.1 which represents a laser beam propagating in the z-direction. In this picture, points P_1 and P_2 are in the same transverse plane (at $z = 0$ cross-section of the laser beam). Also P_1' and P_2' are on the same transversal plane (at $z = L_C$) as well as P_1'' and P_2'' are on the plane $z = L$. The P_1 points are assumed to lie on the same transversal position of the beam cross-section (i.e. only the z-coordinate changes, x and y stay constant). Thus they can be understood as representing the electric field at different times in the same transversal position $E(P_1, t)$, $E(P_1, t')$ and $E(P_1, t'')$ (this is because the field at $E(P_1'', t)$ has propagated from the space-time point $(P_1, t-\Delta t) = (P_1, t-(P_1''-P_1)/c)) = (P_1, t'')$. Similar logic applies to the points P_2.

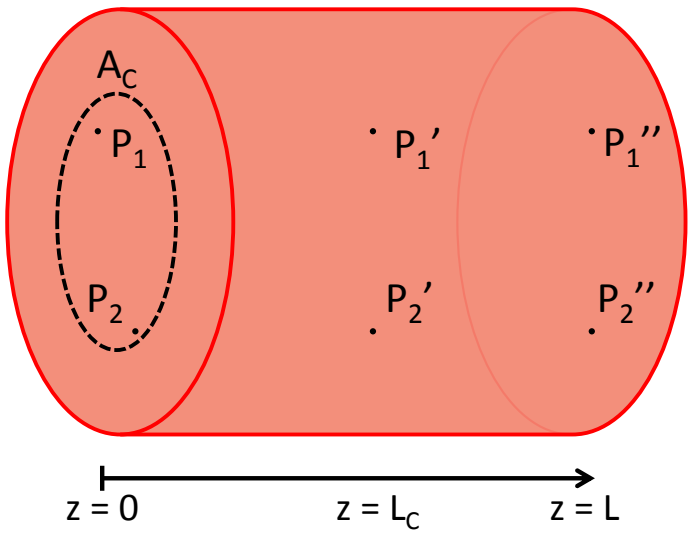

Figure 3.1: Schematic illustration of coherence.

Now we ask the question, are the fields $E(P_1, t)$, $E(P_1'', t)$ and $E(P_1'', t)$ correlated? If we can say that the field at $E(P_1, t)$ depends highly on the field at $E(P_1', t)$ (i.e. we can calculate what the field will be after a time $\Delta t = (P_1'' - P_1)/c$ from the knowledge of the value of the field at time t) the light is *temporally coherent* in the interval from t to $t + \Delta t$. However, if the field $E(P_1'', t)$ does not depend at all on the field at $E(P_1, t)$ (for example because of a random phase jump caused by quantum fluctuations in the laser) it is incoherent in this interval. If the maximum time interval over which the electric fields are correlated is the time it takes for light to propagate from P_1 to P_1' it is called the *coherence time* $t_C = \Delta t$ [64]. Thus coherence time defines the maximum time after which we can predict the electric

field associated with the laser light (i.e. the time that the field stays correlated). We can also calculate the distance light would travel during this time $L_C = ct_C$, which is referred to as the coherence length.

Besides asking ourselves, how does the field correlate with itself at different instants of time (or equivalently different longitudinal coordinates P_1 and P_1''), an equally valid question is how does the field correlates between different transversal parts of the beam? Thus we are comparing the fields at $E(P_1, t)$ and $E(P_2, t)$. Again if they are correlated, and we can deduce the field at P_2 from the value of the field at P_1 we say the light is *spatially coherent*. The are over which the electric field of different points are fully correlated is defined as the *coherence area* A_C.

3.2 First order coherence, fringe visibility

Having introduced the basic ideas behind coherence, we now turn to means of measuring and defining it in a mathematically rigorous way. First we note that any analysis in optics can be performed either in the frequency (spectral) or time-domain, and the same applies to coherence theory and Fourier transformations can be exploited similarly to switch between the two domains. Thus we will use descriptions in both domains depending on the relation to actual measurements.

Traditionally the methods for measuring coherence are based on observing and characterizing interference fringes. For determining spatial coherence properties one inserts two pinholes in the beam cross-section and observes how the fringe pattern varies as the hole spacing is varied. Temporal coherence properties are on the other hand usually obtained by using a Michelson interferometer and observing the intensity fringes as a function of delay between the two arms of the interferometer. In both of these cases the physically measurable quantity is the *visibility* of the interference fringes defined as [64]

$$V(\mathbf{r}/\tau) = \frac{I_{max} - I_{min}}{I_{max} + I_{min}}, \tag{3.2}$$

where $V(\boldsymbol{r}/\tau)$ is the visibility measured in the spatial or temporal domain as discussed above. We neglect the spatial coherence properties of the light from here on, as the system studied in the thesis is single-mode and the SC generated in the fiber is thus perfectly spatially coherent.

We next introduce the first order spectral coherence function defined as [21]

$$g_{12}^{(1)}(\omega) = \frac{\left\langle \tilde{E}_i(\omega)\tilde{E}_j^*(\omega)\right\rangle_{i\neq j}}{\left\langle \left|\tilde{E}(\omega)\right|^2\right\rangle} = \frac{\left\langle \tilde{E}_i(\omega)\tilde{E}_j^*(\omega)\right\rangle_{i\neq j}}{\langle S(\omega)\rangle}, \tag{3.3}$$

where $\tilde{E}_i(\omega)$ and $\tilde{E}_j(\omega)$ represent the electric field associated with different SC

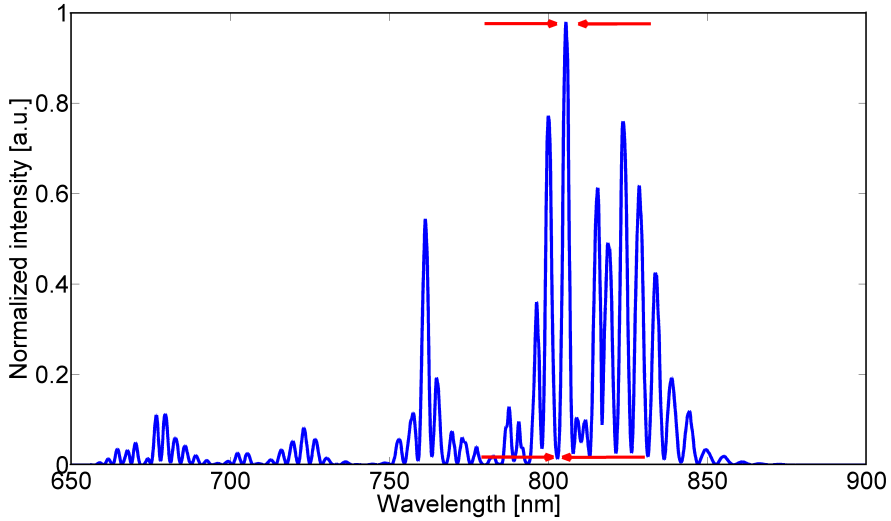

Figure 3.2: Example of a spectral interference pattern measured for a highly coherent SC. The visibility is calculated with the help of consecutive peaks and valleys of the interference pattern marked with red arrows.

pulse realizations.

We will later refer to $g_{12}^{(1)}(\omega)$ with the shorter notation $g_{12}^{(1)}$ the superscript highlighting the fact that it is a first order coherence function. The angle brackets $\langle\rangle$ indicate an ensemble average over independent ($i \neq j$) field realizations. We note that this quantity could be equivalently defined in time domain just by replacing ω with τ. This formulation with the help of ensemble averaging is convenient because it can be used with pulsed and CW light sources. In the CW case (stationary process) the ensemble averaging can be replaced by a time average of the process [64]. In the above equation the absolute value $|g_{12}^{(1)}|$ is actually equal to the fringe visibility of equation 3.2 measured in the spectral domain (i.e. using a delayed Michelson setup with a spectrometer as the detector) [64]. The values of $|g_{12}^{(1)}| = V$ are bound by values 0 and 1 with the first value referring to incoherence and latter to complete coherence. An example of measured spectral interference pattern from which $|g_{12}^{(1)}|$ can be infered is illustrated in figure 3.2

Because the equation deals only with correlations at a certain single frequency (time instant) between realizations, it is referred to as a *first order coherence function*. It thus describes how the electric field of a laser pulse at a certain frequency changes between different pulses. If the laser is stable and the electric field does not fluctuate in amplitude and phase at this frequency between consecutive pulses (or ensemble realizations), the source is coherent. It cannot however describe how the field correlates between different frequencies.

3.3 Second order coherence

Even for non-stationary light sources, such as SC, some insight can be gained from the first order coherence function. However useful additional information can be obtained by *second order coherence functions*. A first order function relies on measuring correlations at the same frequency (time) of independent realizations, whereas the second order functions measure correlations between two different frequencies (times) between different realizations[64].

3.3.1 Mutual Coherence Function and Cross Spectral Density

We define the two-time mutual coherence function (MCF) as [64]

$$\Gamma(t_1, t_2) = \langle E(t_1)E^*(t_2)\rangle = \int_{-\infty}^{\infty}\int_{-\infty}^{\infty} E_1 E_2^* p(E_1, t_1; E_2, t_2) dE_1 dE_2. \tag{3.4}$$

The last form is a general formulation of the ensemble average, given here just to illustrate the relation to correlation functions (i.e. the indefinite integrals), here the $p(E_1, t_1; E_2, t_2)$ represents the joint probability density function [64]. For convenience the coordinates of the system may be transformed from the absolute time (t_1, t_2) to average and difference coordinates $(\bar{t} = (t_1 + t_2)/2, \Delta t = t_2 - t_1)$. The MCF is then transformed into

$$\Gamma(\bar{t}, \Delta t) = \langle E(\bar{t} + \Delta t/2)E^*(\bar{t} - \Delta t/2)\rangle \tag{3.5}$$

This is often normalized in a manner similar used for the first order coherence function,

$$\gamma(\bar{t}, \Delta t) = \frac{\Gamma(\bar{t}, \Delta t)}{\sqrt{I(\bar{t} + \Delta t/2)I(\bar{t} - \Delta t/2)}} \tag{3.6}$$

Here $I(t) = \Gamma(\bar{t}, \Delta t = 0)$ is the ensemble average intensity of realizations. The width (FWHM) of $|\gamma(\bar{t}, \Delta t)|$ along the Δt axis is related to the coherence time at an instant $\bar{t}$ [27]. The MCF has a spectral domain counterpart called the cross-spectral density (CSD) function, defined in average and difference frequency coordinates as

$$W(\bar{\omega}, \Delta\omega) = \left\langle \tilde{E}(\bar{\omega} + \Delta\omega/2)\tilde{E}^*(\bar{\omega} - \Delta\omega/2)\right\rangle. \tag{3.7}$$

It also has a normalized form

$$\mu(\bar{\omega}, \Delta\omega) = \frac{W(\bar{\omega}, \Delta\omega)}{\sqrt{S(\bar{\omega} + \Delta\omega/2)S(\bar{\omega} - \Delta\omega/2)}}. \tag{3.8}$$

It's worth noting that all of the above functions are two dimensional. Furthermore

the non-normalized MCF and CSD in equations 3.5 and 3.7 form a dual Fourier transform pair, however the normalized functions $\gamma(\bar{t}, \Delta t)$ and $\mu(\bar{\omega}, \Delta\omega)$ do not posess this property in the general case [64]. Both are normalized forms, bound in absolute value similarly to $|g_{12}^{(1)}|$ between 0 and 1. Clearly, if one is able to determine either one of the MCF or CSD, it gives access to information in both domains. The CSD is in general more accessible by experimental measurements (by the ease of optical spectrum measurement) and hence we demonstrate most of the results with the help of the CSD as no additional transformations are required.

Overall degree of coherence

To give an overall estimate of the degree of coherence the *overall degree of spectral coherence* $\bar{\mu}$ is used. It represents a kind of an average coherence over the CSD normalized by the average spectrum in a way that it becomes bounded in the interval $0 \leq \bar{\mu} \leq 1$. It is evaluated by the equation

$$\bar{\mu}^2 = \frac{\int_{-\infty}^{\infty}\int_{0}^{\infty} |W(\bar{\omega}, \Delta\omega)|^2 \, d\bar{\omega} d\Delta\omega}{\left[\int_{0}^{\infty} S(\omega)\right]^2}. \tag{3.9}$$

In a very similar manner an overall degree of temporal coherence $\bar{\gamma}$ can be calculated with the help of the MCF. It can be shown that $\bar{\gamma} = \bar{\mu}$ [27] and thus we do not explicitly define it here.

4. SUPERCONTINUUM AND SECOND ORDER COHERENCE

The possible effect of noise in SC generation has become obvious in chapter two describing the nonlinear mechanisms causing the spectral broadening. This randomness in the SC generation process makes it a so called stochastic non-stationary process. We introduced the tools for analysing correlations in such systems in chapter 3 and this chapter employs them for studying the coherence properties of SC. Even though randomness is present in SC generation, it does not mean it would be a completely (temporally/spectrally) incoherent light source fluctuating significantly between realizations (we emphasize again that spatial coherence properties can be neglected in a single-mode fiber). Indeed the effect of noise varies depending on the experimental parameters and coherent, stable, SC can be obtained.

From numerical simulations point of view this noise effect can be accounted for. As it was mentioned in section 2.2, the numerical models employ a random noise seed at the beginning of a single simulation and multiple simulations are done to produce an ensemble of realizations. Often an ensemble of 100-1000 realizations is sufficient to bring out the characteristics observed in experiments, where the number of realizations per one observation is in the order of millions when using typical MHz repetition rate Ti:Sapphire laser oscillators. Thus we have the means to study the coherence properties of SC experimentally as well as numerically.

Before turning into the more mathematical analysis, we discuss what does coherence of SC mean and introduce some rule-of-thumb generalizations on determining the coherence properties of SC.

4.1 Supercontinuum coherence

The early studies [21] to determine SC coherence employed only the first order coherence function $g_{12}^{(1)}$ of equation 3.3. Experimentally the measurement is performed by a delayed Michelson interferometer, where the delay between the two arms matches separation between consecutive laser pulses resulting in spectral interference measured by a spectrometer or optical spectrum analyzer (OSA). In this case the spectral interference pattern resulting from two independent (and consecutive) SC generated is measured.

At frequencies where the fringes visibility is high, the generated SC electric field

amplitude and phase remains nearly constant from shot to shot. On the other hand if the visibility is low there are significant fluctuations in the SC. These fluctuations are caused by noise amplification dynamics during SC generation as discussed below. In short, if consecutive SC spectra resemble each other the coherence is high. On the other hand if consecutive SC spectra vary a lot it's said to be incoherent (note that we cannot measure a single spectrum experimentally, but this can be verified by simulations).

Although the use of the first order coherence function gives a fairly good picture of the overall coherence. A complete second order coherence measurement is required to be able to study for example the behavior of SC in optical systems.

4.2 Effect of pulse duration and peak power on coherence

4.2.1 Pulse duration

We first consider the effect of varying the pulse duration. We assume that the peak power of the pulse remains fixed. As mentioned, TBP ties the temporal duration and spectral width together: shortening the pulse in time increases the bandwidth and *vice versa*. For short pulses below 50 fs duration the FWHM bandwidth is on the order of tens of nanometers.

In these short pulse cases the soliton fission process is deterministic when pumping in the anomalous dispersion regime (as done in the experiments of this thesis) [10]. The dominant process in the beginning is SPM causing spectral broadening [10]. This means that the FWM and SRS gain bandwidths usually overlap with the laser pulse bandwidth, leading to coherent growth of the sidebands with respect to the center wavelength and thus the soliton fission process also occurs in a coherent manner. If the laser pulse-to-pulse fluctuations at the fiber input are small this will lead to consecutive SC to be identical and thus being highly coherent.

At the other extreme we consider pulses of durations of picoseconds and longer up to CW operation. In these cases the pulse bandwidth is initially narrow and symmetrical sidebands around the pump grow from noise seeded by the FWM/MI processes [10]. This means that consecutive spectra vary significantly, and the coherence is typically low.

In the 100 fs ... 1 ps range the coherence can vary remarkably from coherent to partially coherent to entirely incoherent, caused by competition between the noise driven MI effects with the deterministic soliton fission process. The significance of other parameters such as the location of the ZDW relative to the pump wavelength and the peak power grow in these cases. One way to ensure coherence is to pump in the normal dispersion regime, where soliton fission and FWM/MI processes are prohibited. However this comes at a cost of maximum attainable bandwidth as SPM

is the main mechanism of spectral broadening. [10]

4.2.2 Pulse peak power

We next examine the effect of varying the peak power keeping the pulse duration fixed. This can be easily done in practice with a half-wave plate and polarizer combination.

Generally speaking, increasing the peak power leads to a loss of coherence. The reason behind this can be understood again by looking at the FWM/MI gain bandwidth at different peak powers of figure 2.5. The maximum gain shifts further away from the pump wavelength as the peak power is increased. Because of this mismatch between the laser and MI gain spectrum bandwidth, sidebands are seeded by noise. SPM broadening is not able to compensate for this shift and the soliton fission process is perturbed by noise driven MI effects leading to shot-to-shot variations in the fission process. Even though a low peak power allows higher coherence, the downside is that the resulting SC bandwidth is limited.

Finally we note the nearly binary behavior of the overall SC coherence on varying the peak power. As was noted in ref. [24] (see figure 4.1 below), the overall degree of coherence defined in eq. 3.9 stays near unity for low powers but then experiences a rapid drop to values below 0.3 when the peak power is increased and noise starts to influence. The cases where the overall degree of coherence drops rapidly (and has values $\approx 0.2 - 0.8$) is referred as *partially coherent* SC.

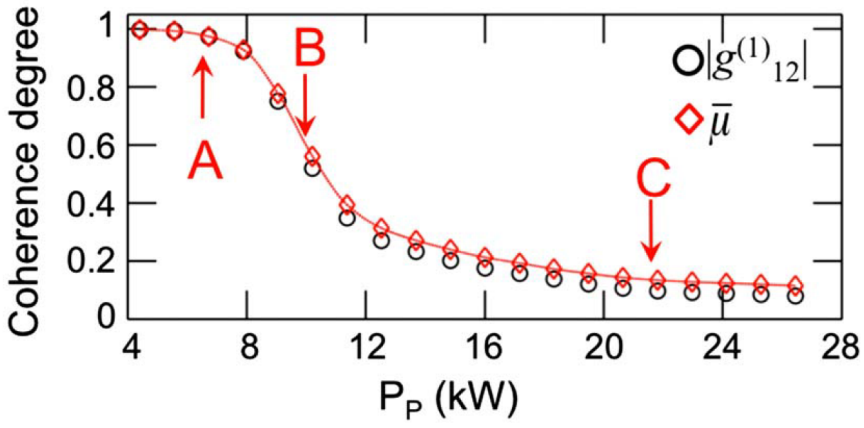

Figure 4.1: Second order overall degrees of spectral coherence $\bar{\mu}$ (red) and first order $|g_{12}^{(1)}|$ (black) for various pumping powers. Case A corresponds to complete coherence, B partially coherent and C incoherent. The drop in overall coherence is rapid near point B. Image taken from ref. [27]

4.3 Separation into coherent and quasi-stationary parts

It has been shown, that the second-order coherence functions of SC can be separated into two distinct contributions: a *quasi-coherent square (cs)* and *quasi-stationary (qs)* part [24]. The separation into these parts in the normalized MCF and CSD representations is illustrated in figure 4.2 below.

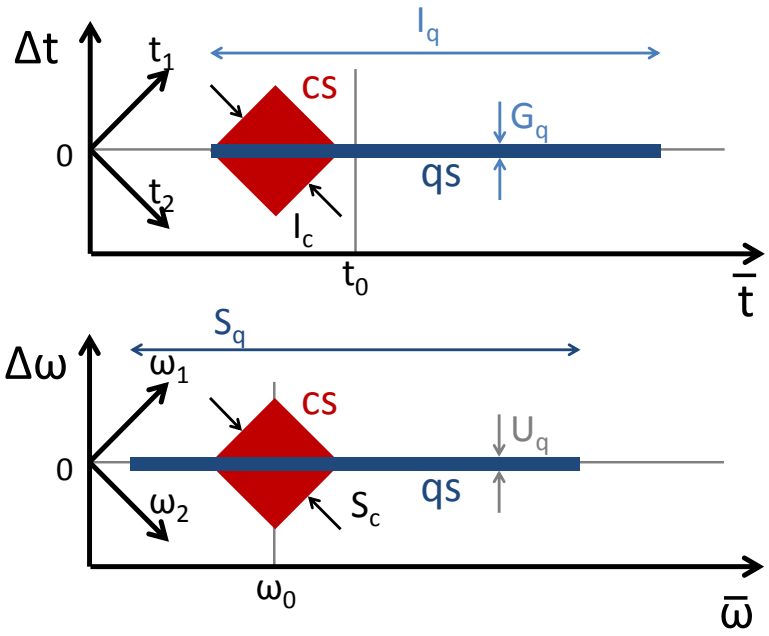

Figure 4.2: Illustration of separation of the (absolute value of) a) normalized MCF ($|\gamma(\bar{t}, \Delta t)|$) and b) CSD ($|\mu(\bar{\omega}, \Delta\omega)|$) functions into cs and qs parts.

The cs-part corresponds to a square part in the normalized CSD(MCF), where the value is nearly unity representing perfect coherence. The qs-part on the other hand is represented by a line in the average frequency (time) direction with nearly constant width in the difference frequency direction so that the coherence properties only depend on the time (or frequency) difference. The separation appears to be valid for any combination of pump pulse and fiber parameters (duration, peak power, wavelength) [24].

The separation can then be used to approximate the normalized MCF and CSD functions as follows:

$$\begin{aligned} \gamma(\bar{t}, \Delta t) &= \gamma_c(\bar{t}, \Delta t) + \gamma_q(\bar{t}, \Delta t) \\ \mu(\bar{\omega}, \Delta\omega) &= \mu_c(\bar{\omega}, \Delta\omega) + \mu_q(\bar{\omega}, \Delta\omega), \end{aligned} \tag{4.1}$$

where the subscripts c and q correspond to the coherent square and quasi-stationary parts, respectively. The separation can be extended to $\Gamma(\bar{t}, \Delta t)$ and $W(\bar{\omega}, \Delta\omega)$ by

simple multiplication according to equations 3.5 and 3.7

Coherent part

Because $\gamma_c(\bar{t}, \Delta t)$ and $\mu_c(\bar{\omega}, \Delta\omega)$ represent fully coherent contributions they can be written in a similar form as the total CSD and MCF of equations 3.5 and 3.7 but without the ensemble averaging. The averaging can be left out because the coherent part does not fluctuate from shot to shot by definition. Replacing $\tilde{E}(\omega)$ with $\tilde{E}_c(\omega)$ and $E(t)$ with $E_c(t)$ we can then write:

$$\begin{aligned} \mu_c(\bar{\omega}, \Delta\omega) &= \frac{\tilde{E}_c(\bar{\omega} + \Delta\omega/2)\tilde{E}_c{}^*(\bar{\omega} - \Delta\omega/2)}{\sqrt{S_c(\bar{\omega} + \Delta\omega/2)S_c(\bar{\omega} - \Delta\omega/2)}} \\ \gamma_c(\bar{t}, \Delta t) &= \frac{E_c(\bar{\omega} + \Delta\omega/2)E_c^*(\bar{\omega} - \Delta\omega/2)}{\sqrt{I_c(\bar{t} + \Delta t/2)I_c(\bar{t} - \Delta t/2)}}. \end{aligned} \tag{4.2}$$

The replacement mentioned above is justfied, if we assume that the fields can be separated to coherent and quasi-stationary parts, where they satisfy the conditions

$$\begin{aligned} I(t) = \Gamma(t,t) = I_c(t) + I_q(t) = |E_c(t)|^2 + |E_q(t)|^2 \\ S(\omega) = W(\omega,\omega) = S_c(\omega) + S_q(\omega) = |\tilde{E}_c(\omega)|^2 + |\tilde{E}_q(\omega)|^2. \end{aligned} \tag{4.3}$$

The coherent parts of the intensities and spectra can be retrieved from the $\pm 45^o$ cross-sections of the cs-parts (illustrated by I_c and S_c in figure 4.2) [24].

Looking at figure 4.1 it is fairly clear that the polychromatic spectral coherence function $g_{12}^{(1)}$ is closely related to the overall degree of coherence and thus the CSD. It was shown in a recent publication [27] that the coherent part of the normalized CSD function can be approximated with the help of the first order coherence function of equation 3.3 as

$$|\mu_c(\omega_1, \omega_2)| \approx \sqrt{|g_{12}^{(1)}(\omega_1)||g_{12}^{(1)}(\omega_2)|}. \tag{4.4}$$

Thus we have the experimental access to the $|\mu_c|$ through this approximation.

Quasi-Stationary part

For the quasi-stationary part we assume that it describes a field with intensity $I_q(\bar{t})$ varying slowly with $\bar{t}$ compared to the variation of $|\gamma_q(\bar{t}, \Delta t)|$ with respect to Δt (i.e. $I_q >> G_q$ in fig. 4.2). This allows the approximation $\Gamma_q(\bar{t}, \Delta t) \approx I_q(\bar{t})\gamma_q(\Delta t)$ to be made. Similar arguments (i.e. $S_q >> U_q$) apply in the frequency domain, allowing

us to write $W_q(\bar{\omega}, \Delta\omega) \approx S_q(\omega)\mu_q(\Delta\omega)$. The quasi-stationary contributions, now approximated as one-dimensional distribution being constant over the average time (frequency) direction, can be calculated directly through 1-d Fourier transforms:

$$\begin{aligned} \mu_q(\Delta t) &= \frac{1}{E_0}\int_{-\infty}^{\infty} I_q(\bar{t})exp(i\Delta\omega\bar{t})d\bar{t}, \\ \gamma_q(\Delta\omega) &= \frac{1}{2\pi E_0}\int_{-\infty}^{\infty} S_q(\bar{\omega})exp(-i\bar{\omega}\Delta t)d\bar{\omega}. \end{aligned} \tag{4.5}$$

where $E_0 = (2\pi)^{-1}\int_{-\infty}^{\infty} I(t)dt$ is the total pulse energy.

4.4 Supercontinuum coherence representation

The above approximations have been verified through numerical simulations, where the exact MCF and CSD can be determined. By the use of the approximations, we can experimentally access the second order coherence function for SC light. Before discussing the experimental methods for determining the CSD and MCF in more detail in the following chapter, we will briefly take a look in two other representations of the CSD and MCF functions. We will not discuss these topics in depth, as they require involved mathematical analysis. The reason they are included here is to give the reader a hint how the results of the separation could be exploited in practical applications.

4.4.1 Coherent modes

The first of these representation is called the *coherent mode* (CM) representation. Generally, the CSD and MCF (we focus only on the CSD but similar argument can be applied to the MCF) of partially coherent fields can be represented as a linear combination of fully coherent fields [65; 64].

$$W(\omega_1, \omega_2) = \sum_{n=1}^{\infty} \lambda_n \psi_n^*(\omega_1)\psi_n(\omega_2) \tag{4.6}$$

where the $\psi_n(\omega)$ represent fully coherent fields or coherent modes and λ_n are the corresponding eigenvalues satisfying the eigenvalue equation of the form

$$\int_0^{\infty} W(\omega_1, \omega_2)\psi_n(\omega_1)d\omega_1 = \lambda_n\psi_n(\omega_2). \tag{4.7}$$

Each term of the sum in eq. 4.6 actually represents the CSD of single coherent field. Thus one can think that we are expressing the total partially coherent CSD as a sum of individual coherent CSDs.

The CSD and MCF functions can be used to model light propagation in linear

optical systems (i.e. providing insight into SC behavior in various measurement setups) [64]. However this can be computationally demanding and simplification by the CM representation can greatly decrease the complexity of calculations [66]. This is based on the fact that the above infinite summation can be first of all truncated to a finite number of terms and secondly that the calculations of involving coherent fields are faster compared to that of fields of partial coherence [66].

4.4.2 Elementary field representation

The number of required modes for the truncated CM representation to be accurate varies greatly depending on the coherence properties of the SC field. For cases with high coherence, even the first mode gives an accurate approximation whereas for cases with low coherence more than 100 modes might be required [66].

Even though this can still reduce the computational complexity compared to the full CSD analysis, another method called the *elementary field* (EF) representation can be employed to further simplify the calculations [67].

The EF method for supercontinuum makes use of the aforementioned observation of dividing the complete CSD into the qs and cs parts and constructs two (quasi-coherent) elementary fields weighted by weight functions to approximate the CSD (similarly to eq. 4.3). To introduce this concept we follow the time-domain analysis of the MCF as in ref. [68].

Applying the decomposition of eq. 4.1 we can write the two-time MCF as

$$\begin{aligned}\Gamma(t_1,t_2) = &\int_{-\infty}^{\infty} p_c(t')E_c^*(t_1-t')E_c(t_2-t') \\ &+ \int_{-\infty}^{\infty} p_q(t')E_q^*(t_1-t')E_q(t_2-t').\end{aligned} \tag{4.8}$$

Here the first term on right denotes the coherent part and the second term the quasi-stationary part of the MCF. The E_c, E_q are the elementary fields and p_q, p_c their associated weight functions. Note that here we have used the non-normalized version of the MCF decomposition which is easily obtained by multiplying eq. 3.6 by the average intensity.

If the coherent part is assumed to be completely coherent, allowing us to assume the weight function to be binary, we can further write [68]

$$\begin{aligned}\Gamma(t_1,t_2) = &E_c^*(t_1)E_c(t_2) \\ &+ \int_{-\infty}^{\infty} p_q(t')E_q^*(t_1-t')E_q(t_2-t').\end{aligned} \tag{4.9}$$

The validity of this approximation is somewhat questionable in partially coherent SC cases where the coherent square has values significantly less than unity. However for the fully coherent and incoherent cases (remember the nearly binary behavior of SC coherence mentioned in section 4.2.2) this approximation is generally valid.

Now the elementary fields describing the coherent and quasi-stationary parts of the above equation can be obtained from the temporal intensity of the coherent part and spectrum of the quasi-stationary part (because of the separation of eq. 4.3) with the help of the equations

$$\begin{aligned} E_c(t) &= \sqrt{I_c(t)}exp[i\phi_c(t)] \\ E_q(t) &= \int_{-\infty}^{\infty} \sqrt{S_q(\omega)}exp(-i\omega t)d\omega. \end{aligned} \tag{4.10}$$

From an experimental point of view, the phase information $\phi_c(t)$ is generally lost, but in principle it could be retrieved with the help of the average spectrum of the coherent part using a phase-retrieval algorithm [68]. The second equation is the Fourier transform of the spectrum of the quasi-stationary part. As the phase of this part is random, no retrieval is required here.

The weight function p_q is connected to the quasi-stationary intensity according to our earlier decompositions through

$$I_q(t) = \int_{-\infty}^{\infty} p_q(t')|E_q(t-t')|^2 dt'. \tag{4.11}$$

With the assumption that p_q is generally real and nonnegative the above equation can be inverted yielding p_q explicitly [69]. Thus by determining $I_q(t)$,$I_c(t)$ and $S_q(\omega)$ we are able to construct the elementary fields.

In reference [68] a comparison between the CM and EF representations for propagating SC light in a linear system (single-mode fiber) was also performed. The results showed that the CM results in general a much more accurate picture of the system behavior but the EF yields comparatively good approximations in the completely coherent and incoherent cases. Because of the simpler and computationally less demanding approach provided by the EF, it could be the preferred representation in the incoherent cases where the number of required modes for CM can easily exceed one hundred.

5. EXPERIMENTAL MEASUREMENT OF SUPERCONTINUUM SECOND ORDER COHERENCE

Having introduced the 2nd order coherence functions, the possibilities to approximate them and utilize for applications we now turn to their actual measurement. The analysis is straightforward to implement for simulations but an exact CSD is impossible to build from experimental data. This is because (with current techniques) single shot electric field (in time or frequency) is impossible to measure.

However the separation into the distinct coherent and quasi-stationary contributions allows to determine approximatively the second order coherence functions experimentally.

5.1 Separation to coherent and quasi-stationary parts experimentally

Coherent part

As mentioned previously, the coherent part can be approximated with the help of equation 4.4. This argument can be readily verified from figure 5.1, where the exact CSDs from simulations are compared to CSDs constructed with the approximation above. One can immediately notice the resemblance of the two. It is also evident from the figure that for the coherent cases (insets a) and b)) there is nearly one-to-one correspondence whereas when the coherence decreases $g_{12}^{(1)}$ cannot reproduce the quasi-stationary line but is still able to reproduce the coherent square.

The $|g_{12}^{(1)}|$ function can be readily accessed experimentally by measuring the visibility of the fringes from the interference spectrum between the two arms of a delayed Michelson interferometer as mentioned in section 3.2.

Quasi-stationary part

To gain access to the quasi-stationary contribution of the CSD, one can make use of equations 4.5. The average temporal intensity $I(t)$ of the SC can be determined experimentally using cross-correlation frequency-resolved optical gating (XFROG) [70].

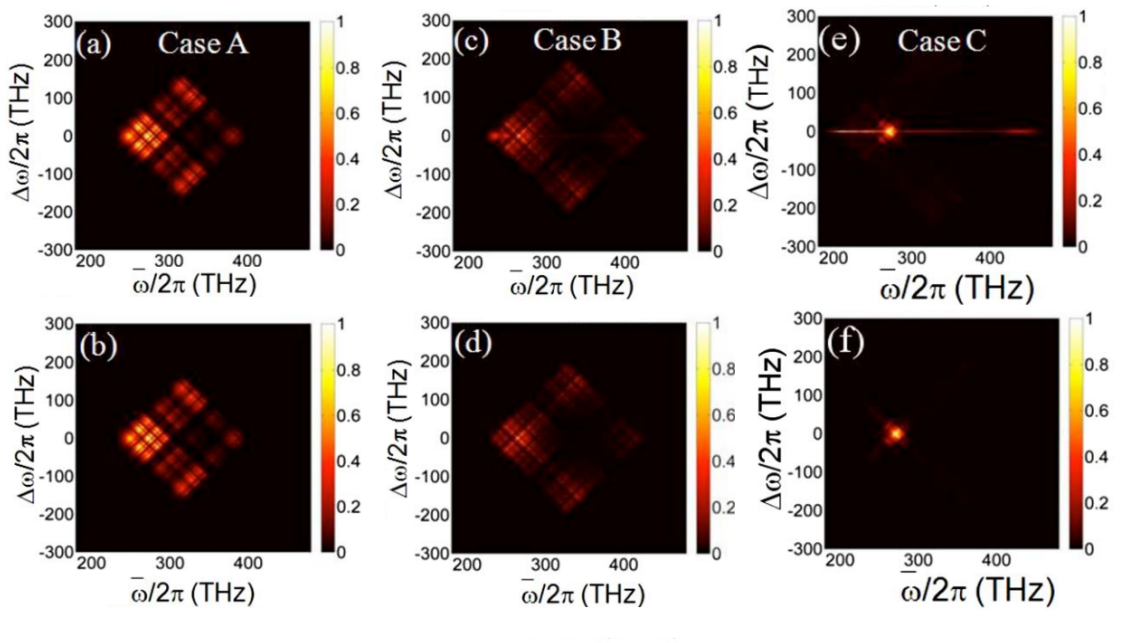

Figure 5.1: **Top row**: Exact CSDs $|\mu(\bar{\omega}, \Delta\omega)|$ calculated for a) coherent case, c) partially coherent and e) in coherent case corresponding to the cases in figure 4.1. **Bottom row**: Corresponding approximate CSDs calculated with $|g_{12}^{(1)}|$. Taken from ref. [24].

However, the quasi-stationary contribution of the CSD requires to measure the contribution to the temporal intensity $I_q(t)$ of the quasi-stationary part. This can be retrieved from the XFROG spectrogram and the spectral coherence function $g_{12}^{(1)}$ following the procedure desccribed below and illustrated in figure 5.2.

1. Filter out the coherent contribution to the 2-D spectrogram by multiplying with $(1 - |g_{12}^{(1)}|)$ along the time axis which isolates the incoherent part in the spectrogram representation.

2. Integrate the filtered spectrogram over the frequency axis essentially which gives the intensity corresponding to $I_q(t)$ (Actually, this is a convolution$I_q(t)$ with the XFROG reference pulse. The validity of this approximation is assessed in the section covering XFROG.)

3. Perform the FT according to eq. 4.5.

We have described above how to reconstruct the CSD from distinct experimental measurements. Because of the direct connection to the spectral coherence function, it is also possible to construct the MCF from the measured data. The coherent contribution to the MCF can be calculated from $|\Gamma_c(t_1, t_2)| = \sqrt{I_c(t_1) I_c(t_2)}$. The coherent part of the temporal intensity is directly obtained from the XFROG spectrogram since $I_c(t) = I(t) - I_q(t)$ and the qs contribution is obtained by Fourier

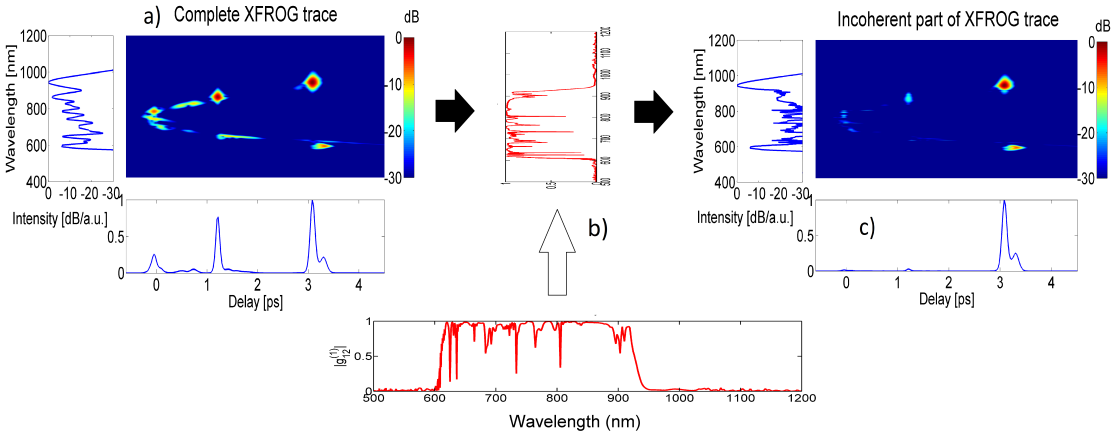

Figure 5.2: Procedure to retrieve $I_q(t)$ from an XFROG spectrogram. Start with the 2-D spectrogram of inset a), filter it out with the help of the coherence function of b). From the remaining spectrogram, integrate over the frequency axis to get $I_q(t)$ illustrated in c).

transformation of the filtered spectrum $S_q(\omega) = S(\omega) \times (1 - |g_{12}^{(1)}|)$ (see eq. 4.5).

The different pathways to recover the different domain coherence functions is illustrated in figure 5.3.

5.1.1 Phase retrieval of coherence functions

The CSD and MCF are in general complex-valued functions and so far we have only been plotting the absolute values of these functions. In experiments, we can only measure modulus of the complex values and cannot access the phase of the data. Even though μ_q obtained by the preceeding procedure is complex because of the FT performed to retrieve it, the phase obtained in this manner has no real physical significance.

This is a common problem (e.g. electron microscopy, astronomy, holography, FROG [71]) in physics and mathematics. This is an inversion-problem that requires usually the use of algorithms to retrieve the phase. Furthermore, one-dimensional phase retrieval problems are well-known to be ill-posed and having only trivial, infinitely many or no solutions [72; 70].

On the other hand, the support constraints in a two-dimensional phase retrieval problem provide usually enough information for one to be able to solve the phase retrieval problem [71; 70]. Even though it's a well studied problem, there are no universal algorithms that work for all the cases. We next introduce two of the most general algorithms, which are typically modified to suit the exact problem at hand.

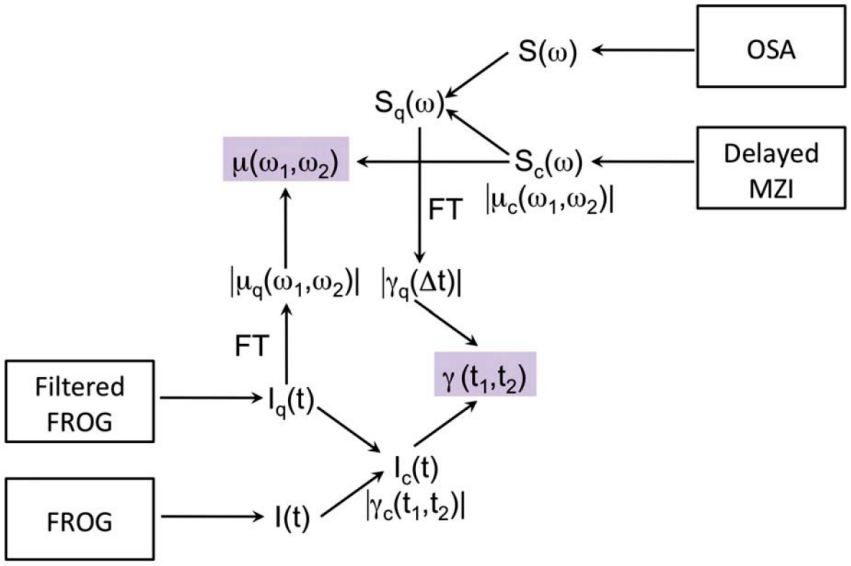

Figure 5.3: The different experimental parts required and a flow-chart to determine either the CSD or MCF experimentally. OSA:Optical spectrum analyzer, MZI: Mach-Zehnder interferometer which can be replaced with a Michelson interferometer. Taken from ref. [27].

Gerchberg-Saxton algorithm

As mentioned previously, we have access to both the MCF and CSD modulus data experimentally. As the non-normalized MCF and CSD form a FT pair we can switch between these domains while enforcing the measured modulus data after each FT. Because the FT gives a complex result, one hopes that the phase information gets closer to the actual solution after each cycle of FTs and forcing the modulus data in both domains. This is the basic principle behind the Gerchberg-Saxton(GS) algorithm [73].

A modification of this algorithm was actually used in the early FROG experiments [74]. The FROG measurement setup allows for additional constraints to be imposed, improving convergence. For FROG measurements the convergence of the algorithm has been further improved by applying principal value decomposition methods [75].

In the absence of additional constraints the basic GS algorithm converges rather poorly with even simulated data. So far for the CSD phase retrieval convergence has been reached only with an initial phase guess constructed of the correct phase with added random phase. For experimental cases, the convergence is expected to be even worse because of the noise inevitably present in the modulus data.

Hybrid Input-Output algorithm

Another workhorse in phase-retrieval is the Hybrid Input-Output (HIO) algorithm introduced by Fienup [76]. It also makes use of the Fourier transform property, but instead of enforcing modulus data in both domains, it only does it in either of the domains. The algorithm starts with an initial guess (which can be in our case the modulus of the CSD) with a (random) phase seed. It then performs the FT, enforces the MCF modulus data followed with an inverse FT. The output CSD is then compared to the original CSD and corrected towards the desired direction. This corrected CSD is then used as a new input followed by a new iteration.

The difficulty here is to define the correction in a way that it would be in the direction of the result. Often, just a simple support constraint is used, where the data outside of the support is set to zero and data inside the support is corrected towards the modulus data. This is a very simplistic method and corresponds nearly to the GS algorithm. However, were one to be able to find a better correction method, improvement of convergence could be expected.

Finally we highlight the possibility of using other phase-retrieval algorithms, such as the Generalized Projections algorithm used in FROG retrieval [75] or genetic algorithms with suitable modifications to the problem. However the phase plots of simulated CSD are very complex and retrieval is expected to be difficult.

5.2 Experimental setup

Separate measurements are needed to determine the modulus value of the CSD. These include a Michelson interferometer and an XFROG system. The XFROG measurement further requires a complementary FROG measurement to characterize the gate pulse used in order to be able to retrieve the temporal intensity properly. The same complementary FROG can also be used to characterize the input pulse injected into the fiber which can be used to make comparative simulations. Thus all in all three distinct components can be recognized in the whole measurement scheme:

1. FROG measurement to determine the gate/input pulse,
2. XFROG measurement to characterize the SC spectral and temporal properties,
3. Delayed Michelson interferometer (DMI) for measuring $|g_{12}^{(1)}|$.

An overall schematic is given in figure 5.4. We next give descriptions of each of these components separately. The setup used in the experiments was slightly different because of practical issues. The differences are not shown in the figure, because we wanted to preserve clarity in the schematic, but the principle of the schematic still holds.

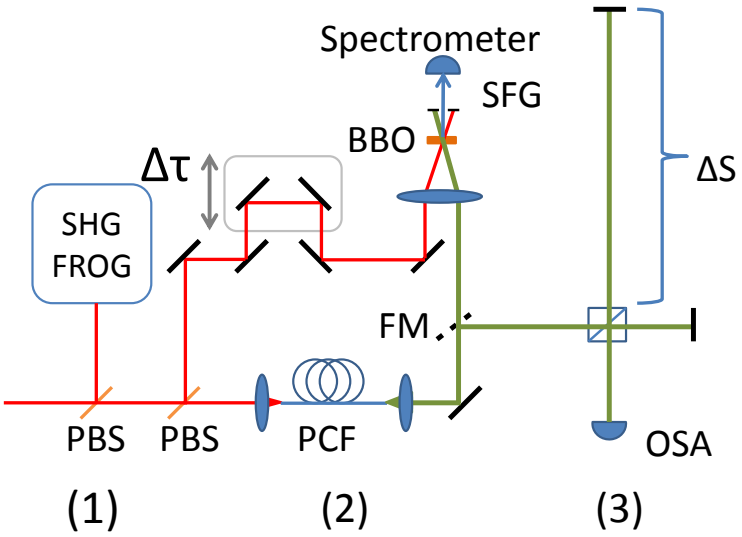

Figure 5.4: Simplified schematic for the experimental setup emloyed in this thesis. Three components are required: 1) SHG FROG , 2) XFROG , 3) Delayed Michelson interferometer. PBS: Pellicle beamsplitter, FM: Flip mirror, BBO: Beta-barium-borate, the second order nonlinear crystal used for frequency mixing, SFG: Sum-frequency generation, PCF: Photonic Cystal Fiber, $\Delta\tau$: variable delay on a motorized stage.

5.2.1 Supercontinuum generation

The SC under study were generated with a Spectra Physics Tsunami Ti:Sapphire laser oscillator with a repetition rate of 80 MHz and pulse energies in the order of nanojoules with an adjustable wavelength. These pulses were divided with a pellicle beamsplitter to obtain the gate pulse for the XFROG and the input pulse to the PCF fiber. The input pulse to the fiber passed through an optical Faraday isolator consisting of approximately 6.5 cm of terbium-gallium-garnet. This caused significant broadening and down-chirp in the input pulse, which also was characterized with SHG FROG. The center wavelength in experiments was 785 nm.

For generating the SC a PCF fiber NL-PM-750 was chosen. It is a polarization-maintaining, highly nonlinear fiber from NKT Photonics. The length of the fiber is 68.5 cm. The nonlinearity, dispersion profile and a scanning electrograph image of this fiber are presented in the chapter 2.4, *Photonic Crystal Fibers*. The dispersion profile used in the simulations was the one provided by the manufacturer and shown in figure 2.9.

The peak power of the input pulse was varied during experiments by rotating a half-wave plate (HWP) in combination in front of a polarizer, right after the optical isolator. A separate HWP was used to couple the light into one of the main polarization axis of the PCF to ensure correspondence with simulations.

5.2.2 Frequency-Resolved Optical Gating

SHG FROG

SHG FROG is an intensity autocorrelation type measurement, where the short pulse is used to sample itself. This is achieved by splitting the pulse into two identical replicas of itself and introducing a variable delay for the other pulse. These pulses are then combined back in a nonlinear crystal where the measured second harmonic signal strength depends on the delay. The signal is at maximum when the pulses overlap perfectly in time and the electric field strength is at maximum causing strong second harmonic signal. When the pulses overlap only a little or not at all, the measured SHG signal is weak. By measuring the signal strength as a function of delay one obtains a picture of the pulse in question. Often a chromatic filter is also implemented in the setup to cut of residual pump power causing possible distortion in the measurement. In our case a dichroic mirror by Semrock with a cutoff wavelength of 510 nm was used.

This method has to be implemented because ultrashort pulses are generally non-measurable even by the fastest photodetectors. But where intensity autocorrelators measure the total intensity with a photodetector, a FROG measurement replaces this with a spectrometer (in our experiments it was the Avantes AvaSpec-ULS2048L StarLine with a resolution of 0.5 nm and variable integration time). Often a non-collinear beam geometry is used as illustrated in figure 5.5 a). In this case a SHG beam is created in the direction of the green beam only when the two pulses overlap in the nonlinear crystal. Thus by systematically changing the delay for the second pulse and measuring the resulting spectrum at the output one constructs a two-dimensional spectrogram of the pulse shown in figure 5.5 b). Mathematically the spectrogram $S(\tau, \omega)$ is of the form

$$S(\tau, \omega) = \left| \int_{-\infty}^{\infty} p(t) g(t+\tau) e^{i\omega t} dt \right|^2 , \tag{5.1}$$

where $p(t)$ is called the *probe pulse* under study and $g(t+\tau)$ is the *gate pulse* used to sample the probe. In the SHG FROG case these two are the same pulse, but the other one is delayed as discussed earlier.

As mentioned in the phase-retrieval algorithms section, a FROG measurement requires also a phase-retrieval to produce accurate results. The acquired spectrogram data are fed to a commercial FROG software made by Femtosoft, which has various algorithms implemented and calculates the results automatically.

Other nonlinearities can be exploited for FROG setups (e.g. THG, self-diffraction) yielding often easier traces to retrieve. SHG FROG was chosen here because of its experimental simplicity and the possibility of using the same nonlinear crystal and

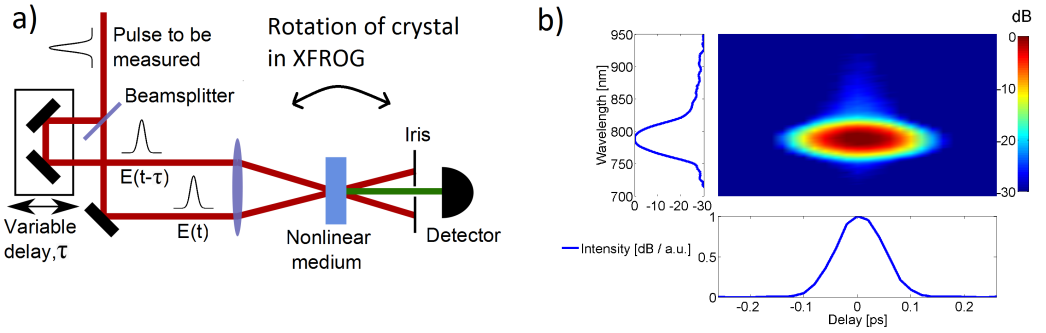

Figure 5.5: a) FROG measurement. b) An example of a measured spectrogram of the pulse produced by the Ti:Sapphire laser used in this work and that serves as the reference pulse for the XFROG measurement. Retrieval yields a pulse with TBP of 0.642 and a FWHM temporal duration of 70 fs. Center wavelength $\lambda_0 = 785$nm.

beam alignment for the XFROG measurement. As the nonlinear crystal a beta-barium borate crystal of thickness 1 mm was chosen to provide sufficient nonlinear conversion efficiency.

XFROG

The principle of XFROG is similar to SHG FROG, but here one uses a well known reference pulse to sample the pulse under study. In our case the characterized laser pulse by the SHG FROG (the gate pulse in eq. 5.1) is used to sample the SC generated in the fiber (the probe pulse in eq. 5.1). These two pulses are then again combined in a second order nonlinear crystal resulting in sum-frequency generation (SFG). This sum-frequency signal is then measured with a spectrometer.

The major differences are firstly that the total delay scanned needs to be longer as the SC often spans durations over picoseconds compared to the laser pulse femtosecond scale. The maximum scan range for experiments was roughly 10 ps, covering the studied SC easily. Secondly, because the SC spectral density is fairly weak, a thick nonlinear crystal is required to achieve measurable sum-frequency signals. This on the other hand leads to limitations in phase-matching for the SFG between the laser pulse and SC and the crystal needs to be rotated quickly to enable phase-matching over the whole SC bandwidth [77].

Attention should be paid to the polarization of the SC such that phase-matching is efficient in the selected nonlinear crystal. In our experiment a HWP was used to select one of the principal axis of polarization of the PCF at the input and the output of the fiber was mounted on a rotational fiber mount to align the polarization so that SFG signal is optimized.

A retrieval is also required in the XFROG measurements. However, in order to be able to retrieve the electric field from the experimental XFROG spectrogram

the gate pulse must be scanned with less than 2 fs steps, corresponding to 0.3 μm displacement in the motorized delay stage. This is due to gridding in the phase-retrieval software that binds the spectral and temporal resolutions together [78]. The stage used in the experiments (ThorLabs DRV-001) was however limited to a minimum step size of 3 μm (corresponding to resolution of 20 fs) and thus a retrieval was not possible.

It should be noted however, that in the incoherent case the retrieval is somewhat irrelevant as the experimental XFROG will consist of an ensemble of very different SC and thus most likely a single electric field cannot be retrieved which would represent the whole ensemble. Even if the mean field could be retrieved, the phase information would be close to useless. In the coherent case, the ensemble would consist of similar fields, and in principle a retrieval could be possible from a mathematical point of view. To study the possibility of using the frequency marginals (integration of the trace over the frequency axis) as a representation for the average intensity $I(t)$, an XFROG trace was calculated numerically for a simulated coherent SC using a gate pulse of 70 fs corresponding to experiments.

It was found that the general characteristics of the XFROG time marginals resembled that of the average intensity well. This is illustrated in figure 5.6. This can be understood easily by noting that the XFROG time-margin is practically the same as a convolution of the average intensity with the gate pulse. As the gate pulse duration is comparable or less than the temporal structures of the SC, the convolution does not change the result significantly. Hence we conclude that when a short enough gate pulse is used, the XFROG time margin can be used to approximate the average intensity.

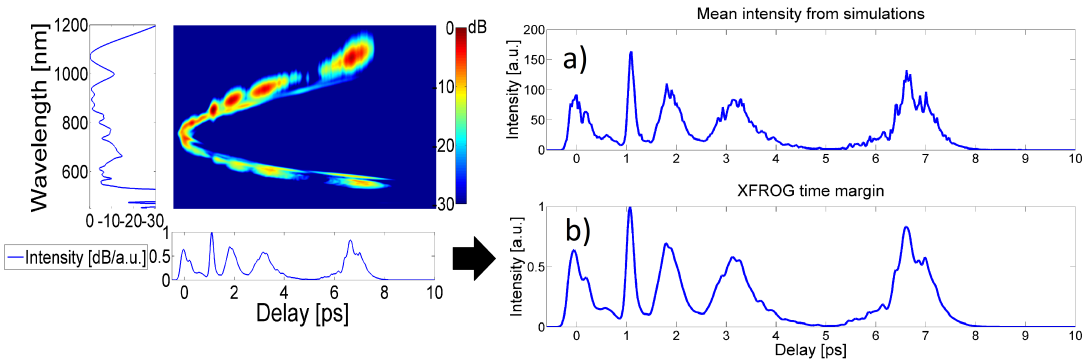

Figure 5.6: Comparison between a) the simulated mean intensity and b) XFROG time margin. With a short gate pulse, the general shape is similar, but the XFROG margin washes out the fine structure.

Finally we highlight that from an experimental point of view decreasing the step size in the measurements (in order to make a retrieval possible) increases the mea-

surement time. As the fiber coupling can vary in practice over long periods (e.g. because of heating of the fiber), this would lead to reliability issues in the measurements. Thus the significance of this alteration needs to be considered carefully. To ensure the coupling efficiency does not vary througout the measurement, the spectrum of the SC should be measured before and after completion of a set of measurements. In a reliable measurement these two would produce identical results.

5.2.3 Delayed Michelson interferometer

The third and final step of the measurement is the DMI that measures the coherence function $|g_{12}^{(1)}|$. As the XFROG measurement requires all available power from the SC and takes a longer time compared to the DMI measurement, the XFROG was measured first and after that a flip mirror was used to reroute the SC beam to the interferometer as shown in fig. 5.4.

The whole idea behind the interferometer lies in the fact that the second interferometer arm is longer by a distance equal to the laser repetition rate $\Delta S = c\tau_{rep}$. This means that we are actually mixing two consecutive, independently created SC (i.e. in equation 3.3 we are enforcing the rule $i \neq j$). The interference fringes are then recorded in the spectral domain by the OSA. The fringe spacing depends on the delay and it determines the measurement resolution. The OSA's superior resolution (the ANDO 6315B with 0.05 nm resolution), allowing for small fringe spacing to be resolved is thus preferred over spectrometers. Fringe spacing was set to approximately 4 nm resulting in points at 2 nm resolution in the $|g_{12}^{(1)}|$ function, which is well above the Nyquist sampling limit of 0.1 nm obtainable with the OSA resolution available. Fringe spacing was set large to ensure the highest possible contrast obtainable of the visibility fringes, rather than sampling close to the limit causing possible loss of contrast.

Because the visibility of the fringes (and hence $|g_{12}^{(1)}|$) is largely affected by beam allignment, mirror stability and focusing into the OSA, extra care needs to be taken to ensure that the actual contrast of the fringes is measured. In a normal Michelson interferometer, this is easily achieved. However, as the propagation lengths vary by a distance of nearly 4 m in our setup, diffraction and mirror stability in the longer arm play an even more crucial role. In practice, even for completely coherent SC with weak powers (only SPM broadened), a value higher than $|g_{12}^{(1)}| = 0.93$ was not measured. Hence it can be argued that the experimentally measured overall degree of coherence value is systematically underestimated compared to the actual values. This should be kept in mind when comparing the experimental results to simulations.

6. RESULTS AND DISCUSSION

The second order coherence properties of SC light corresponding to various overall degrees of coherence were measured using the procedure described in the previous section. These are compared with numerical results simulated with the GNLSE using similar parameters as used in the experiment.

As mentioned, the duration of the injected pulse into the nonlinear fiber to generate SC was different from the gate pulse used for XFROG as it was temporally broadened and strongly chirped after passing through the optical isolator. The input pulse at the fiber input characterized by SHG FROG and the temporal FWHM width for the input pulse was found to be $\approx$ 290 fs with a spectral width of 17 nm. As a comparison the gate pulse for XFROG was found to be $\approx$ 70 fs with an identical spectral width.

For the numerical results, an ensemble of 500 realizations was simulated for each set of input parameters investigated. The simulation grid contained 2^{14} points ($\approx$ 16000) spanning a range of 22 ps resulting in a time resolution of roughly 1 fs and a spectral resolution of 0.05 THz. The step size in the split-step method was about 0.2 mm.

As these resolutions are much higher than our experiments allow, the absolute values of the simulated CSD and MCF were two-dimensionally convolved with a Gaussian function to produce comparable results with experiments. For the CSD a Gaussian with a FWHM of 2 nm was used, corresponding to the fringe spacing in the DMI. As for the MCF the width was chosen to be 70 fs corresponding to the duration of the XFROG gate pulse. Of these two convolutions the MCF experienced a more significant change, whereas the blurring effect on the CSD was more minute.

The simulation parameters were set to match the experimental conditions, with the exception of the peak power which was increased compared to the experimental setup to produce a comparable spectral bandwidth. This is justified, as the power measurement in the experiments performed at the fiber input are underestimated compared to actual power injected into the PCF. The experimentally measured powers were 78%, 65% and 68% of that used in the simulation for the coherent, partially coherent and incoherent cases investigated respectively. The similar values hint further of a systematic error in the experimental power measurement.

Moreover, the typical dispersion profile (fig. 2.9) for the fiber provided by the

manufacturer has a fairly large error margin of ±15 nm for the ZDW. As the pump wavelength is very close to the reported ZDW of 750 nm, even a slight variation in this can cause significant differences in the numerical simulations.

6.1 Highly coherent, narrowband case

We start by looking at a highly coherent case with an experimental peak power of $P_{p,exp} \approx 70$ W. In this case the SC spectrum spans a 220 nm bandwidth from c.a. 650 nm to 870 nm. The corresponding peak power in the simulations was $P_{p,sim} = 90$ W. The measured XFROG spectrogram with its marginals are shown in figure 6.1 and a corresponding figure for simulations is shown in 6.2.

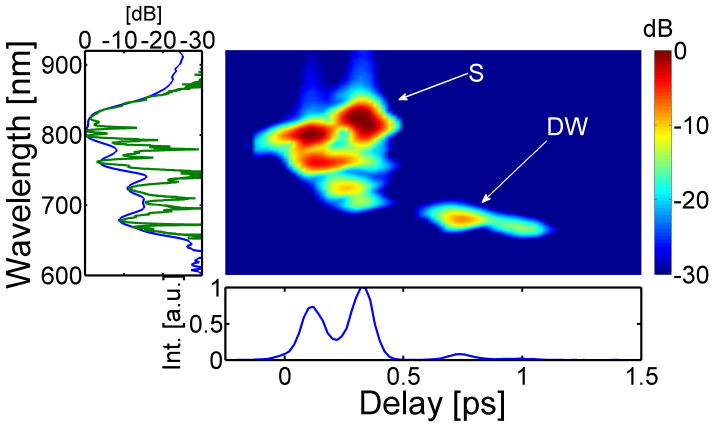

Figure 6.1: Experimental XFROG spectrogram and corresponding marginals for a coherent SC. The green line shows the SC spectrum measured with the OSA which matches the XFROG frequency margins marked with blue. S: Soliton, DW: Dispersive wave.

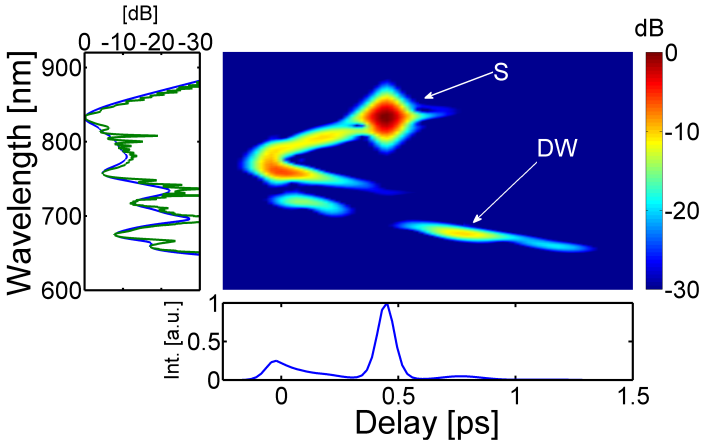

Figure 6.2: Simulated XFROG spectrogram and corresponding marginals for the coherent SC. The green line shows the SC spectrum measured with the OSA which agrees very well with the XFROG frequency margins marked with blue. Soliton S can be observed very clearly.

The XFROG traces share similar distinct characteristics such as the clear soliton ejected by the soliton fission process and the corresponding dispersive wave. The soliton order is $N \approx 6$ for experiments and simulations and the first ejected soliton can be observed clearly red-shifting via SRS. As the peak power is still sufficiently low, soliton fission is highly deterministic as MI noise effects are still nonexistent.

Some differences can be also seen. The soliton at 850 nm has separated further away in time from the pump in the simulations. Furthermore, the soliton intensity seems to be higher in the simulations which can be seen from comparing the time marginals. The spectra share very similar characteristics as do the first order coherence functions $|g_{12}^{(1)}|$. These are shown more accurately in figure 6.3.

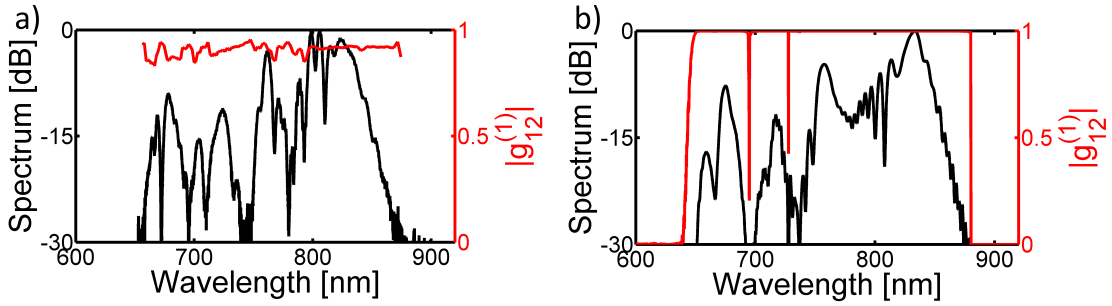

Figure 6.3: Spectrum and corresponding $|g_{12}^{(1)}|$. a) Experimental result with an average value for $|g_{12}^{(1)}|$ of 0.90. b) Simulated result withand average of 0.99.

A very good correspondence can be seen in both the spectra and $|g_{12}^{(1)}|$. As for the first order coherence function, the experimental value never exceeds 0.93 whereas in the simulations it is practically equal to unity at every wavelength. This can be understood by the discussion in the experiments section regarding the high sensitivity to vibrational noise of the DMI measurement.

We further compare the CSD (fig. 6.4) and MCF (fig. 6.5) functions retrieved from the experiments to the ones directly calculated from the simulation ensembles. Both the CSD and MCF are dominated by the cs-part.

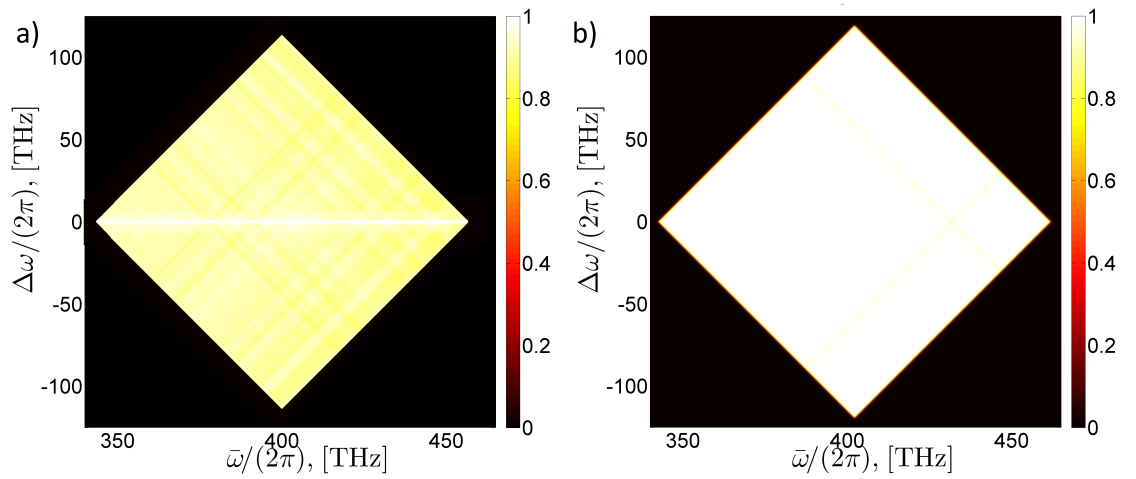

Figure 6.4: a) CSD retrieved from experiments, b) CSD calculated from the simulation ensemble. Second order overall degree of coherence is $\bar{\mu} = 0.93$ and $\bar{\mu} = 0.99$ for a) and b) respectively.

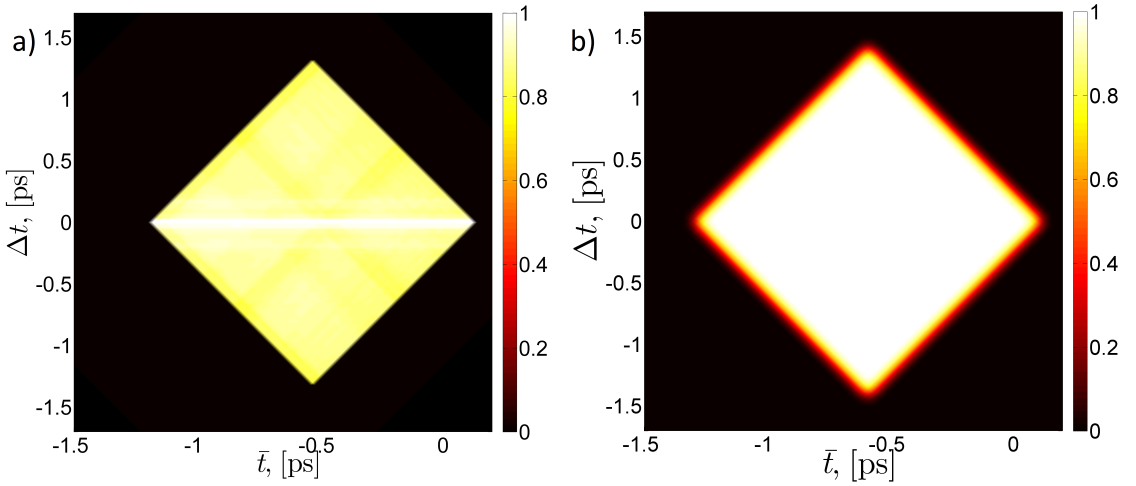

Figure 6.5: a) MCF retrieved from experiments, b) MCF calculated from the simulation ensemble. Second order overall degree of coherence is $\bar{\gamma} = 0.93$ in a) and $\bar{\gamma} = 0.99$ in b).

A good agreement between simulated results and experimentally retrieved results can be seen for both the MCF and CSD, even though the experimental values are slightly lower and not uniform because of the noise. The slight differences in the sizes of the squares are just a result from slightly different temporal extents and spectral bandwidths of the SC.

6.2 Partially coherent case

The peak power was then increased to $P_{p,exp} \approx 360$ W resulting in a partial loss of coherence. The decrease in coherence occurs rapidly within a narrow power range as discussed earlier. This can also be verified experimentally by observing the interference pattern of the DMI while adjusting the half-wave plate and polarizer combination. Below we plot again the experimental (fig. 6.6) and simulated (fig. 6.7) XFROG traces with marginals. The peak power used in the simulations was $P_{p,sim} = 560$W which corresponds to a soliton order of $N = 15$.

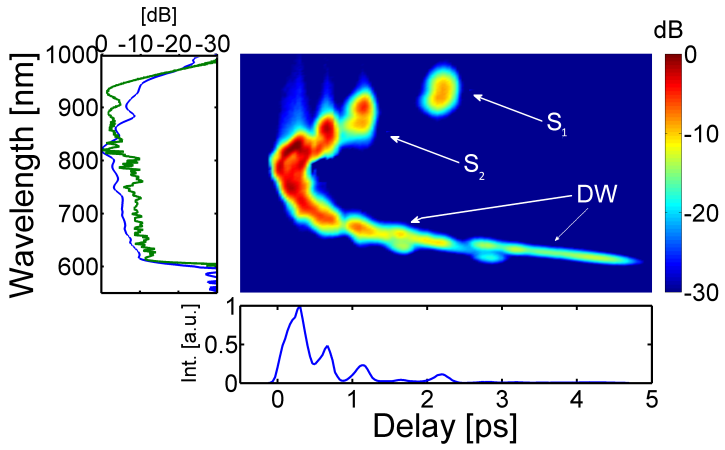

Figure 6.6: Experimental XFROG spectrogram and corresponding marginals for partially coherent SC. The green line shows the SC spectrum measured with the OSA which matches the XFROG frequency margins marked with blue.

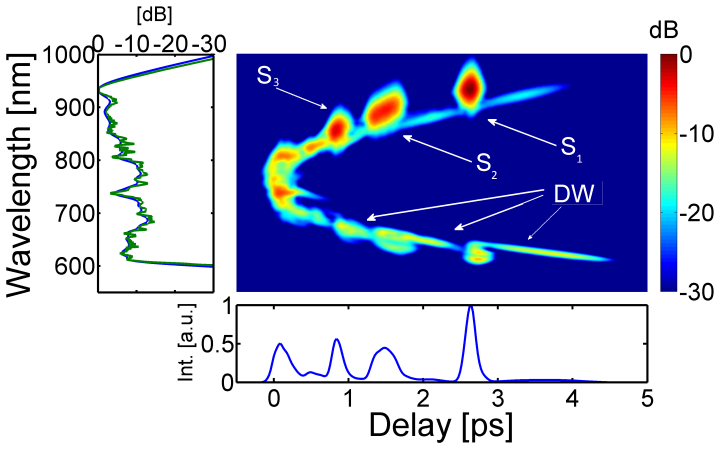

Figure 6.7: Simulated XFROG spectrogram and corresponding marginals for partially coherent SC. In the frequency marginal: green line is the SC spectrum measured with the OSA. Blue line: XFROG frequency margins marked with blue. Three distinct solitons with their corresponding dispersive waves can be seen in the figure.

Again the correspondence is qualitatively vey good between experiments and simulations. The noise driven MI is starting to create spectral sidebands outside the pulse bandwidth effecting soliton fission at these power levels. The random perturbations cause jitter in the soliton locations, both temporally and spectrally. This is seen especially in the blurred S_2 soliton of figure 6.7. On the other hand soliton S_3 is ejected from the pump before MI sidebands have grown significantly and thus is less affected by MI which is why this soliton is not blurred. In both cases three solitons and their dispersive waves can be recongized, even though in experiments the third one is much closer to the pump. The soliton intensities observed in experiments are again lower compared to those in the simulations and they have moved further away in time in the simulations.

The lower intensity of the solitons could possibly be explained by a decreased phase-matching for the extreme wavelengths in experiments. This would explain the differences in the XFROG frequency marginal (blue) and OSA spectrum (green). Even though the crystal is rotated to allow partial phase-matching, the beams are also propagating through different thicknesses of the crystal caused by the non-collinear beam geometry illustrated in fig 5.5. This can cause attenuation of the reference pulse via SHG before interacting with the SC in the crystal.

Indeed, some residual SHG was always present in experiments which was filtered out by substracting a background spectrum recorded in the absence of XFROG signal. However this was not always sufficient, and some residual SHG could still be observed in the XFROG traces. They are not seen in the experimental traces however as they were further filtered out in the parts of the XFROG trace where easily visible. Thus some residual SHG could have artificially increased the intensity at the pump wavelength in the measured traces.

The spectra and $|g_{12}^{(1)}|$ are plotted again in figure 6.8 to inspect the differences more closely.

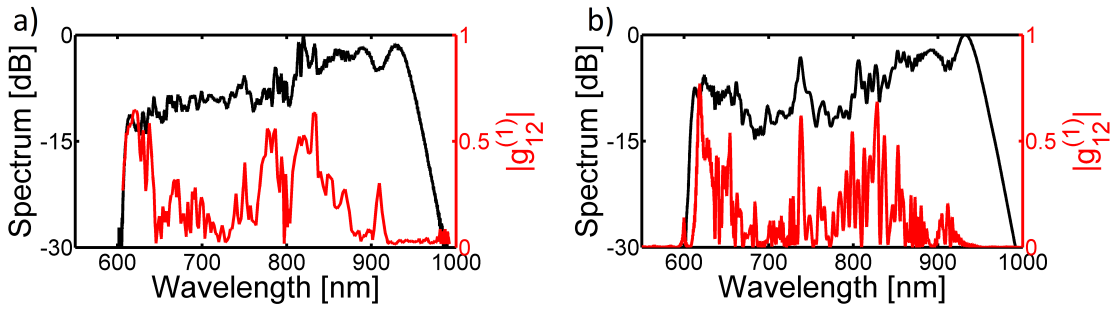

Figure 6.8: Spectrum and corresponding $|g_{12}^{(1)}|$. a) Experimental result with an average value for $|g_{12}^{(1)}|$ of 0.18. b) Simulated result with an average value of 0.16.

The general correspondence is good between experiments and simulations with

the spectral bandwidth being nearly the same in both cases. The simulated spectrum contains however stronger spectral components at around 750 nm. In the experimental case the dispersive wave peak at 600 nm is also less pronounced. This is most likely due to the uncertainty on the dispersion profile of the PCF or non-uniform coupling efficiency of light over the spectrum into the OSA.

The coherence functions $|g_{12}^{(1)}|$ exhibit similar variations. The simulated one contains in general more fine structure, which cannot be observed in simulations. Most likely the correspondence could be improved with a convolution with a Gaussian corresponding to the fringe spacing. Of the similarities worth noting are the peaks at just above 900 nm close to the soliton, the wide interval of higher coherence from 750 nm to 870 nm with a dip in the middle and finally the coherent peak at the low end edge of the spectrum corresponding to the dispersive wave. The center interval is seeded by SPM of the redshifted pump leading to better coherence. MI causes jitter in the soliton positions and consequently in the dispersive waves, leading to a loss of coherence at wavelengths far from the pump. However, at 600 nm the associated dispersive wave for coherent soliton S_3 at 900 nm causes the rises in the $|g_{12}^{(1)}|$ function at these wavelengths.

We next compare the CSD (fig. 6.9) and MCF (fig. 6.10) functions retrieved from experiments to that caluclated directly from the simulations.

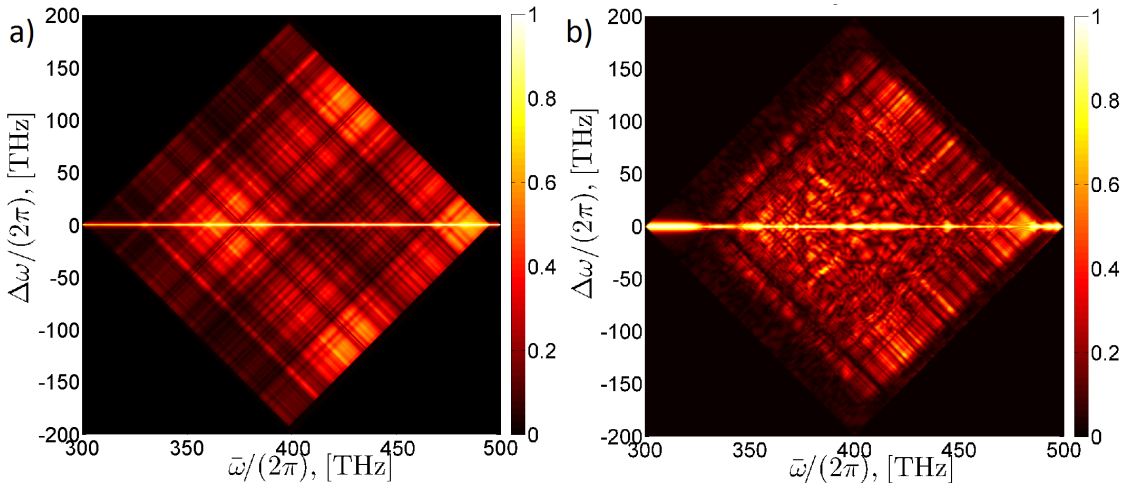

Figure 6.9: a) CSD retrieved from experiments, b) CSD calculated from the simulation ensemble. Second order overall degree of coherence is $\bar{\mu} = 0.25$ and $\bar{\mu} = 0.28$ for a) and b) respectively.

Even though the simulations show much more fine structure, a good general correspondense can be seen, in agreement with the similarity of the $|g_{12}^{(1)}|$ function in the simulations and experiments. Most significant differences can be seen along the axis $\Delta\omega = 0$, with the clearest difference at the low mean frequency $\bar{\omega}$ edge at 320 THz. The simulated CSD contains wider parts in the $\Delta\omega$ direction corresponding

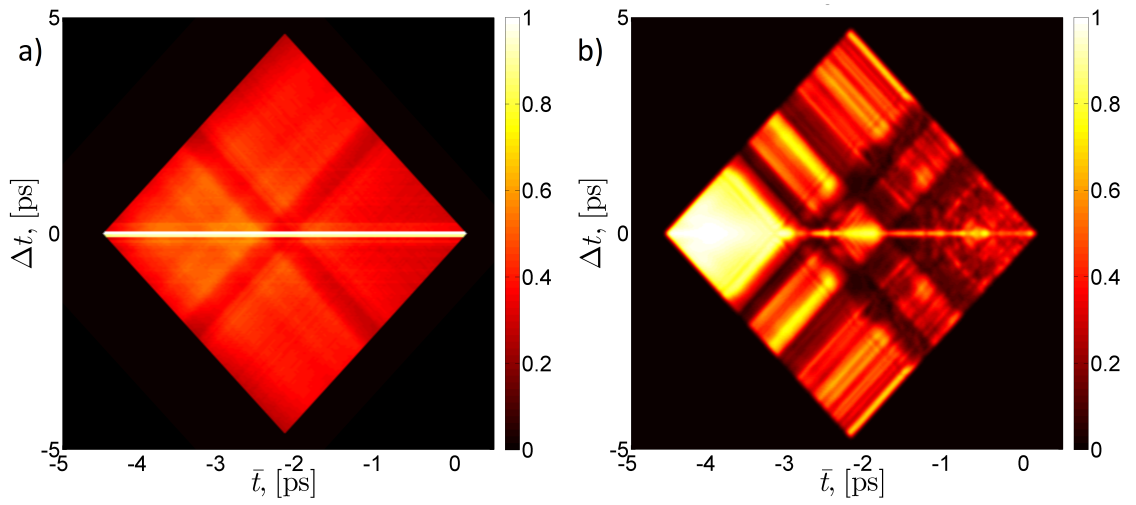

Figure 6.10: a) MCF retrieved from experiments, b) MCF calculated from the simulation ensemble. Second order overall degree of coherence is $\bar{\gamma} = 0.50$ in a) and $\bar{\gamma} = 0.29$ in b).

to correlations between the solitons. These cannot be reproduced well by the qs-approximation used to retrieve the experimental CSD.

The experimental MCF suffers from greater differences. The qs-part is thicker in experiments than simulations and the experimental MCF is much more blurred even after the convolution. Some similarities can be seen nevertheless: the MCFs roughly span a similar square area comparable and both contain a smaller square of higher coherence at $\bar{t} = -3.5$ ps. Only one of the distinctive stripes of the simulated MCF is seen in the experiment crossing at $\bar{t} = -2$ ps. This could again be explained with the lower intensity of the experimental solitons which fail to produce the higher peaks observed outside the coherent square in the simulated MCF. The large difference in overall degree of coherence values further hints that the experimentally determined MCF is not accurate.

6.3 Incoherent, wideband case

The peak power was next increased to $P_{p,exp} \approx 820\text{W}$ ($P_{p,sim} = 1200\text{W}$ in the simulations, soliton order $N = 23$) leading to a SC spectral bandwidth of more than 600 nm and a nearly complete loss of coherence. The corresponding XFROG traces for the experiments and simulations are shown in figures 6.11 and 6.12, respectively.

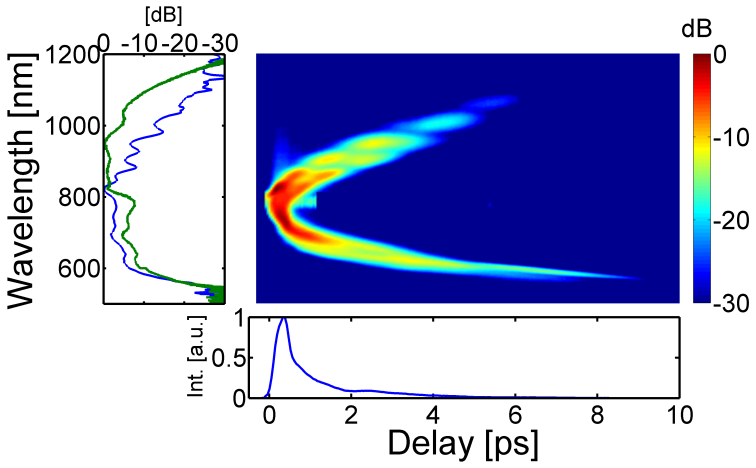

Figure 6.11: Experimental XFROG trace for an incoherent SC.

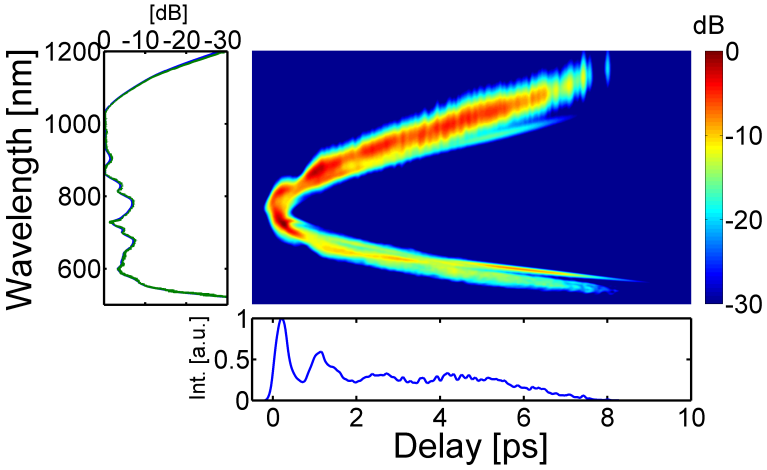

Figure 6.12: Experimental XFROG trace for an incoherent SC.

We immediately notice clear differences to earlier cases and also between simulated and experimental results. With the increased power, initial spectral broadening is caused by MI and even the first ejected solitons will get affected by it leading to a loss of coherence. MI perturbs these solitons differently from shot to shot causing their positions to jitter (spectrally and temporally) significantly in both cases leading to a general blurring effect in the trace. The experimental trace seems to show

however a bit more distinct solitons compared to simulations. Some correlations are seen around the pump wavelength corresponding to some residual SPM processes occuring early on in the propagation.

The experimental solitons seem to disappear entirely after 6 ps delay, whereas in simulations they are observed nearly at 8 ps. Most likely this is again due to the phase-matching problems that cause even stronger attenuation of the measured soliton intensities further away from the pump. It's worth noting that the lower wavelength dispersive waves do not seem to suffer from this as significantly, as can be seen comparing the frequency marginals. On the other hand this can also be due to the abovementioned wavelength dependence of the coupling efficiency to the OSA. Despite the cause, it can be anticipated that the MCF cannot be reproduced very accurately in the experimental case.

Comparing the experimental and simulated spectra and $|g_{12}^{(1)}|$ of figure 6.13 we notice that the spectra are qualitatively well matched with the experiments suffering again from a weaker low wavelength part most likely due to coupling efficiency differences. However for the $|g_{12}^{(1)}|$ a significant difference between experiments and simulations can be observed.

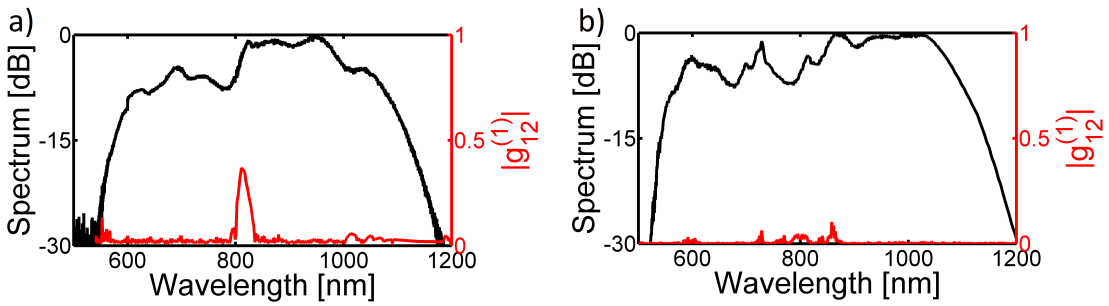

Figure 6.13: a) Experimental spectrum and corresponding $|g_{12}^{(1)}|$ function with an average value of 0.03. b) Simulated spectrum and $|g_{12}^{(1)}|$ function with an average value of 0.006.

Firstly the experimental $|g_{12}^{(1)}|$ is highly localized at around 810 nm, whereas in simulations the residual coherence is more widely spread over the 800nm region with some also seen at 600 nm. Secondly the measured value of $|g_{12}^{(1)}|$ is significantly higher, which is unexpected because of the noise effects mentioned earlier. Even dropping simulation peak power moderately does not produce as high values of $|g_{12}^{(1)}|$. Further dropping the power would cause significant differences in spectral bandwidths between experiments and simulations. Variations in the dispersion profile are known to cause differences in the coherence properties and this could be one possible reason for the discrepancy.

Looking at the CSDs (fig. 6.14) and MCFs (fig. 6.15) clear differences can be noticed as expected from the previous results. The simulated CSD has stripes of

residual coherence crossing at $\bar{\omega} = 375$ THz, whereas the experimental one only contains a less pronounced square around the crossing point.

In both MCFs higher correlations are observed in the cs-part in beginning of the pulse at $\bar{t} = -9$ with the simulational containing more structure. In the experiments the qs-line is normalized to unity and looks very bright. It is also slightly broader than its simulational counterpart. Even though the cs-parts are somewhat comparable in size between simulations and experiment, the values are lower in the experimental one, which can be also seen from the large difference of the overall coherence values. Furthermore the fine structure in other parts of the MCF cannot be observed at all which could be partially caused by the low experimental soliton intensities.

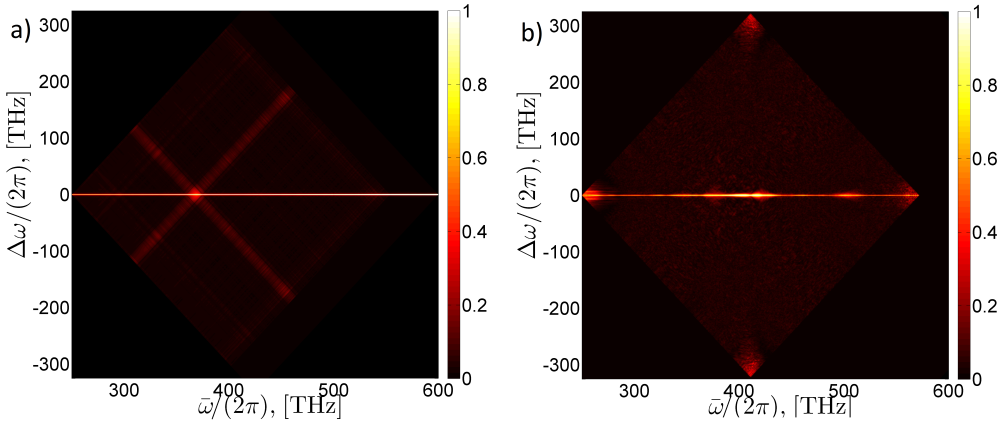

Figure 6.14: Incoherent CSDs from experiments a) compared to the ones from simulations b). Overall degrees of coherence are a) $\bar{\mu} = 0.08$ and b) $\bar{\mu} = 0.01$.

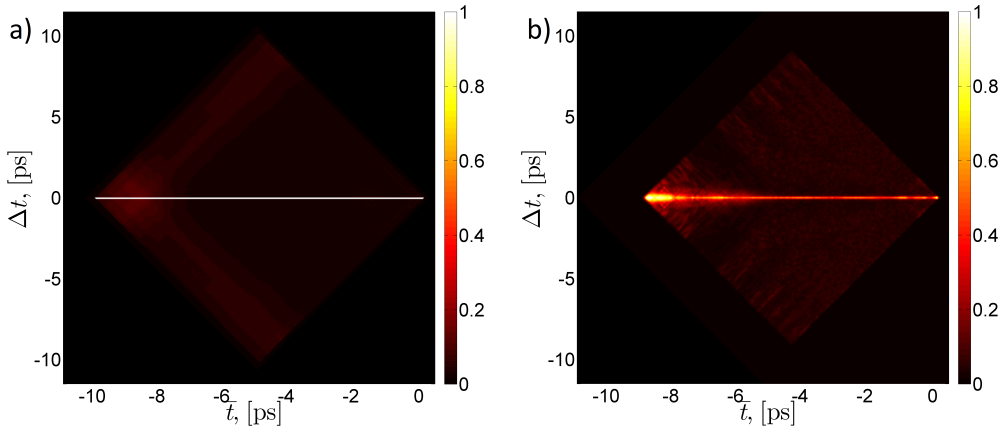

Figure 6.15: Incoherent MCFs from experiments a) compared to the ones from simulations b). Overall degrees of coherence are $\bar{\gamma} = 0.22$ and $\bar{\gamma} = 0.01$ for a) and b) respectively.

6.4 Discussion

Cross-spectral density

The experimental CSD functions show accurately many of the characteristics seen in the simulated counterparts with the overall degree of spectral coherence $\bar{\mu}$ being systematically slightly lower (but comparable) with respect to the simulations except in the incoherent case. This further implies additional noise sources in experiments caused most likely by the vibrations in the DMI or varying coupling efficiency into the PCF caused by heating of the fiber tip. The exact reason of the discrepancy of the CSD in the incoherent case is not known, but it could be due to variations in the actual dispersion profile of the fiber.

Obviously not all of the minute details of the simulated CSD can be reproduced in experiments. One limiting factor (setting aside the noise fluence) is the resolution of the $g_{12}^{(1)}$ function which is most clearly seen in figure 6.8 where the overall shape of simulated $|g_{12}^{(1)}|$ are similar qualitatively but the experimental lacks detail of the simulations. The resolution is set by the fringe spacing set in experiments by fine-tuning the delay. The minimum achievable fringe spacing on the other hand is limited by the OSA resolution. In our experiments the fringe spacing was chosen to be 4 nm yielding points at a resolution of roughly 2 nm. This means that there are 80 points between two peaks with the OSA resolution of 0.05 nm. The large fringe spacing was chosen to yield with certainty the maximum obtainable contrast in the fringe measurement. The spacing could perhaps still be decreased as currently we are sampling about ten times the Nyquist sampling limit.

Mutual coherence function

For the MCF the experimental and simulated correspondence is not as good as for the CSD except in the coherent case. The most likely reason for the observed differences is the fact that the components at the far edges of the spectrum (i.e. solitons and dispersive waves) are of lower intensity in experiments caused probably by a mix of phase-matching problems, large angle differences for the incoming beams and residual SHG from the pump as discussed in the section covering the partially coherent case. The SHG filtering could possibly be enhanced in a simple manner by averaging over more than two background spectra as is done now.

The solutions for the other two problems could possibly be adjusting the setup so that the beams cross at a smaller angle,using a thinner crystal improving phase-matching or measuring (or calculating) the SFG efficiency over the SC bandwidth and then correcting the XFROG trace with this. Using a thinner crystal would decrease the background SHG signal but would also cause the SFG signal strength to drop and should be thus considered in more detail.

The experimental MCF also lacks a lot of detail caused by the accuracy of the temporal intensity retrieved from the XFROG measurement. As discussed and illustrated in fig. 5.6 the XFROG time margin is a fairly good general estimate of the mean temporal intensity, but it loses the fine-structure. This structure cannot be retrieved by a simple deconvolution with the known pulse profile, thus an XFROG retrieval would be needed. This would require a motorized delay stage with a finer step size for the experiments. And as discussed earlier, the possibility of a retrieval for an incoherent SC is uncertain. On the other hand, if an even shorter probe pulse was available for the XFROG, the time margin accuracy would improve even with the current stage.

The inaccuracy of the experimental MCF also inhibits the retrieval of the phase for the CSD and MCF. As convergence of the retrieval is hard to achieve already with simulated results, it is clear that with the current MCF an experimental retrieval is impossible.

Dispersion profile

It is also fairly evident from the results above that the dispersion profile used for the simulations does not exactly correspond to the one in experiments. This can be argued by the fact that in all the cases studied, the temporal stretching in the simulations was systematically larger (i.e. the solitons are further away from the pump) compared to experiments when the spectral width was kept corresponding between the two. Especially the location of the ZDW can cause some variations in coherence properties because of the different dynamics effecting at anomalous and normal dispersion regimes. The effect of varying the ZDW (or pump wavelength) could be studied further to see if even better simulational correspondece could be achieved.

7. SUMMARY AND PERSPECTIVES

An experimental characterization setup for determining supercontinuum second order coherence properties (i.e. shot-to-shot variations) was successfully built. The method is based on separating the SC into coherent and quasi-stationary parts and determining them separately. The separation approximation was made in recent publications based on numerical results and the experimental results presented in this thesis are the first measurements of the second order coherence characteristics of SC light.

As a conclusion for all the three cases a qualitatively good correspondence between simulations and experiments can be observed for the XFROG traces, spectra and CSD functions verifying the separation theory experimentally. Remarkable was the surprisingly good reconstruction of the CSD in the partial coherent case, which has the most difficult characteristics to reproduce. The MCF function reconstruction did not succeed as well in experiments due to a likely problem in SFG phase-matching. Some minor differences in details between simulations and experiments do occur and these are further separated and discussed below with some notes on possible experimental improvements given in the same context.

We have experimentally verified the separation to the qs and cs-parts as argued with the support of numerical simulations in earlier publications. An overall good correspondence between the simulations and experiments was observed. Of course the separation is just an approximation and thus the details of the CSD/MCF from simulations are lost. From an experimental point of view the separation works specially well in the spectral domain CSD because of the ease of measuring $g_{12}^{(1)}$ and its connection to the cs part. Improvements in the MCF measurement could be expected with changes in the experimental setup as discussed below.

The qs-part tends to be wider to the difference coordinate directions in the experimental results. The accuracy of this could possibly be also improved with a higher quality delay stage or a shorter pulse and correcting the phase-matching of the XFROG traces. However, even with a new delay stage, the variations in the qs thickness cannot be reproduced with the current approximation at all.

7.1 Future perspectives

In section 4.4.2 we have discussed the EF representation for the MCF and its application as describing SC performance in optical systems. As it should be clear by now, it could be similarly done for the CSD, and we look at this possibility because of the superior properties of the experimental CSD compared to the MCF. Now one would require knowledge of $S_q(\omega), S_c(\omega)$ and $I_q(t)$ to do the EF construction. The absolute values of the first two are fairly straightforward and accurate to determine from experiments as discussed. However the accuracy of $I_q(t)$ measurement could limit the possibility to determine the required weight function accurately.

Even a more significant problem is the currently impossible phase retrieval for $S_c(\omega)$ because of the inaccurate MCF. Experimentally these problems could be overcome with the following approaches done either together or separately. Firstly, a motorized delay stage with a step size in the order of 0.3μm would make the XFROG retrieval at least theoretically possible. Secondly if a probe pulse with a temporal width of < 20 fs (corresponding to current minimum step size) would be available, a better resolution in the XFROG time margin could be achieved. Of these two, obviously the first choice is more readily implemented as stages with accuracies of 10 nm are available whereas robust few cycle pulsed lasers are more expensive and would require larger adjustments in the current setup. A third and the most straightforward approach expected to improve results dramatically is the correction of the XFROG trace with an experimentally or analytically determined phase-matching efficiency curve. After overcoming the experimental problems a robust phase-retrieval algorithm for the coherence functions needs to be developed.

Even though a proof-of-principle for experimental measurement of the CSD and MCF was shown, it is clear that these measurements are still too complicated to be implemented robustly on a day-to-day basis in applications. Thus the experimental characterization of SC sources at will and using the results for modeling propagation in commercial applications is still far, but not impossible.

With the increased accuracy by taking some of the measures noted above, the EF representation with an experimental setup described could be well used to model SC propagation in linear optical systems used in various imaging techniques. Only for the partially incoherent case this could prove to be problematic as the EF is inherently less accurate in these cases. The increased noise in measurements could enhance the inaccuracy. From an applicational point of view, this should not be a very limiting factor, as most of the applications require either coherent or incoherent light where the EF representation works.

It could also prove to be interesting to study in more detail the cause for the much higher coherence value in experiments compared to simulations near the pump

wavelength in the incoherent case. The behavior seen the experimental data is quite unexpected because of the inherent experimental noise usually causing degradation of coherence compared to simulations. The dispersion profile of the fiber used in experiments compared to that of in the simulations could be a reason for this behavior. However, in light of brief tests of varying the dispersion profile of the fiber in the simulations failed to reproduce the phenomenon and a more rigorous study would be required.

In summary, even if the experimental measurement is not yet entirely accurate, it was again shown that the simulations are able to reproduce experimental results accurately and the separation is generally valid, hence it is justified to use simulations and the EF or CM formalism for application design.

REFERENCES

[1] R. Alfano and S. Shapiro, "Emission in the region 4000 to 7000 angstrom via four-photon coupling in glass," *Phys. Rev. Lett.*, vol. 24, pp. 584–587, 1970.

[2] O. Svelto, *Principles of Lasers*, 5th ed. Springer, 2010.

[3] T. Brabec, C. Spielmann, P. F. Curley, and F. Krausz, "Kerr lens mode locking," *Opt. Lett.*, vol. 17, no. 18, pp. 1292–1294, 1992.

[4] F. Krausz, M. Fermann, T. Brabec, P. Curley, M. Hofer, M. Ober, C. Spielmann, E. Wintner, and A. Schmidt, "Femtosecond solid-state lasers," *Quantum Electronics, IEEE Journal of*, vol. 28, no. 10, pp. 2097–2122, 1992.

[5] J. C. Knight, T. A. Birks, P. S. J. Russell, and D. M. Atkin, "All-silica single-mode optical fiber with photonic crystal cladding," *Opt. Lett.*, vol. 21, no. 19, pp. 1547–1549, 1996.

[6] T. A. Birks, W. J. Wadsworth, and P. S. J. Russell, "Supercontinuum generation in tapered fibers," *Opt. Lett.*, vol. 25, no. 19, pp. 1415–1417, 2000.

[7] W. Wadsworth, J. Knight, A. Ortigosa-Blanch, J. Arriaga, E. Silvestre, and P. Russell, "Soliton effects in photonic crystal fibres at 850 nm," *Electronics Letters*, vol. 36, no. 1, pp. 53–55, 2000.

[8] S. Coen, A. H. L. Chau, R. Leonhardt, J. D. Harvey, J. C. Knight, W. J. Wadsworth, and P. S. J. Russell, "White-light supercontinuum generation with 60-ps pump pulses in a photonic crystal fiber," *Opt. Lett.*, vol. 26, no. 17, pp. 1356–1358, 2001.

[9] G. Genty, M. Lehtonen, H. Ludvigsen, J. Broeng, and M. Kaivola, "Spectral broadening of femtosecond pulses into continuum radiation in microstructured fibers," *Opt. Express*, vol. 10, no. 20, pp. 1083–1098, 2002.

[10] J. M. Dudley, G. Genty, and S. Coen, "Supercontinuum generation in photonic crystal fiber," *Rev. Mod. Phys.*, vol. 78, pp. 1135–1184, 2006.

[11] A. V. Husakou and J. Herrmann, "Supercontinuum generation of higher-order solitons by fission in photonic crystal fibers," *Phys. Rev. Lett.*, vol. 87, p. 203901, 2001.

[12] J. Dudley and G. Genty, "Supercontinuum light," *Physics Today*, vol. 66, pp. 29–24, 2013.

[13] T. K. Laurila, S.-S. Kiwanuka, J. H. Frank, and C. F. Kaminski, "Broadband cavity-enhanced spectroscopy using supercontinuum radiation," in *Lasers, Sources, and Related Photonic Devices*. Optical Society of America, 2012, p. LT5B.4.

[14] P. Ryczkowski, A. Nolvi, I. Kassamakov, G. Genty, and E. Hæggström, "High-speed stroboscopic imaging with frequency-doubled supercontinuum," *Opt. Lett.*, vol. 38, no. 5, pp. 658–660, 2013.

[15] A. F. Fercher, K. Mengedoht, and W. Werner, "Eye-length measurement by interferometry with partially coherent light," *Opt. Lett.*, vol. 13, no. 3, pp. 186–188, 1988.

[16] K. L. Corwin, N. R. Newbury, J. M. Dudley, S. Coen, S. A. Diddams, K. Weber, and R. S. Windeler, "Fundamental noise limitations to supercontinuum generation in microstructure fiber," *Phys. Rev. Lett.*, vol. 90, p. 113904, 2003.

[17] A. Demircan and U. Bandelow, "Supercontinuum generation by the modulation instability," *Optics Communications*, vol. 244, pp. 181–185, 2005.

[18] S. B. Cavalcanti, G. P. Agrawal, and M. Yu, "Noise amplification in dispersive nonlinear media," *Phys. Rev. A*, vol. 51, pp. 4086–4092, 1995.

[19] P. Drummond and J. Corney, "Quantum noise in optical fibers. i. stochastic equations," *JOSA B*, vol. 18, no. 2, pp. 139–152, 2001.

[20] B. Washburn and N. Newbury, "Phase, timing, and amplitude noise on supercontinua generated in microstructure fiber," *Optics Express*, vol. 12, no. 10, pp. 2166–2175, 2004.

[21] J. M. Dudley and S. Coen, "Coherence properties of supercontinuum spectra generated in photonic crystal and tapered optical fibers," *Opt. Lett.*, vol. 27, no. 13, pp. 1180–1182, 2002.

[22] I. Zeylikovich, V. Kartazaev, and R. R. Alfano, "Spectral, temporal, and coherence properties of supercontinuum generation in microstructure fiber," *J. Opt. Soc. Am. B*, vol. 22, no. 7, pp. 1453–1460, 2005.

[23] M. Bertolotti, L. Sereda, and A. Ferrari, "Application of the spectral representation of stochastic processes to the study of nonstationary light radiation: a tutorial," *Pure and Applied Optics: Journal of the European Optical Society Part A*, vol. 6, no. 2, p. 153, 1997.

[24] G. Genty, M. Surakka, J. Turunen, and A. T. Friberg, "Second-order coherence of supercontinuum light," *Opt. Lett.*, vol. 35, no. 18, pp. 3057–3059, 2010.

[25] B. Kibler, J. Dudley, and S. Coen, "Supercontinuum generation and nonlinear pulse propagation in photonic crystal fiber: influence of the frequency-dependent effective mode area," *Applied Physics B*, vol. 81, no. 2-3, pp. 337–342, 2005.

[26] N. Nikolov, T. SÃ¸rensen, O. Bang, A. Bjarklev, and J. Rasmussen, "Modelling of supercontinuum generation in highly nonlinear photonic crystal fibres," *Journal of Optical and Fiber Communications Reports*, vol. 5, no. 1-6, pp. 1–21, 2008.

[27] G. Genty, M. Surakka, J. Turunen, and A. T. Friberg, "Complete characterization of supercontinuum coherence," *J. Opt. Soc. Am. B*, vol. 28, no. 9, pp. 2301–2309, 2011.

[28] J. Manassah, P. Ho, A. Katz, and R. Alfano, "Ultrafast supercontinuum laser source," *Photonics Spectra*, vol. 18, pp. 53–59, 1984.

[29] G. Agrawal, *Nonlinear fiber optics*, 5th ed. Academic press, 2013.

[30] C. Kao, "Sand from centuries past: send future voices fast," Nobel lecture in physics, 2009.

[31] G. Agrawal, *Fiber-optic communication systems*, 3rd ed. Academic press, 2002.

[32] U. Utzinger and R. R. Richards-Kortum, "Fiber optic probes for biomedical optical spectroscopy," *Journal of Biomedical Optics*, vol. 8, no. 1, pp. 121–147, 2003.

[33] D. J. Richardson, J. Nilsson, and W. A. Clarkson, "High power fiber lasers: current status and future perspectives," *J. Opt. Soc. Am. B*, vol. 27, no. 11, pp. B63–B92, 2010.

[34] T. A. Birks, J. C. Knight, and P. S. Russell, "Endlessly single-mode photonic crystal fiber," *Opt. Lett.*, vol. 22, no. 13, pp. 961–963, 1997.

[35] C. Rolland and P. B. Corkum, "Generation of 130-fsec midinfrared pulses," *JOSA B*, vol. 3, no. 12, pp. 1625–1629, 1986.

[36] A. Weiner, *Ultrafast optics*. John Wiley and Sons, 2009.

[37] R. Boyd, *Nonlinear optics*, 3rd ed. Academic press, 2008.

[38] A. Hasegawa and F. Tappert, "Transmission of stationary nonlinear optical pulses in dispersive dielectric fibers. i. anomalous dispersion," *Applied Physics Letters*, vol. 23, no. 3, pp. 142–144, 1973.

[39] L. F. Mollenauer, R. H. Stolen, and J. P. Gordon, "Experimental observation of picosecond pulse narrowing and solitons in optical fibers," *Phys. Rev. Lett.*, vol. 45, pp. 1095–1098, 1980.

[40] J. Satsuma and N. Yajima, "B. initial value problems of one-dimensional self-modulation of nonlinear waves in dispersive media," *Progress of Theoretical Physics Supplement*, vol. 55, pp. 284–306, 1974.

[41] M. Erkintalo, "Nonlinear instabilities and extreme wave localization in fiber optics," Doctoral thesis, Tampere University of Technology, 2011.

[42] F. M. Mitschke and L. F. Mollenauer, "Discovery of the soliton self-frequency shift," *Opt. Lett.*, vol. 11, no. 10, pp. 659–661, 1986.

[43] N. Akhmediev and M. Karlsson, "Cherenkov radiation emitted by solitons in optical fibers," *Phys. Rev. A*, vol. 51, pp. 2602–2607, 1995.

[44] J. D. Harvey, R. Leonhardt, S. Coen, G. K. L. Wong, J. Knight, W. J. Wadsworth, and P. S. Russell, "Scalar modulation instability in the normal dispersion regime by use of a photonic crystal fiber," *Opt. Lett.*, vol. 28, no. 22, pp. 2225–2227, 2003.

[45] M. Yu, C. J. McKinstrie, and G. P. Agrawal, "Modulational instabilities in dispersion-flattened fibers," *Phys. Rev. E*, vol. 52, pp. 1072–1080, 1995.

[46] J. Dudley and J. Taylor, *Supercontinuum generation in Optical fibers*. Cambridge University Press, 2010.

[47] D. Skryabin and A. Yulin, "Theory of generation of new frequencies by mixing of solitons and dispersive waves in optical fibers," *Phys. Rev. E*, vol. 72, pp. 1547–1549, 2005.

[48] D. F. Grosz, C. Mazzali, S. Celaschi, A. Paradisi, and H. Fragnito, "Modulation instability induced resonant four-wave mixing in wdm systems," *Photonics Technology Letters, IEEE*, vol. 11, no. 3, pp. 379–381, 1999.

[49] C. Raman, "A new radiation," *Indian Journal of Physics*, vol. 2, pp. 387–398, 1928.

[50] R. H. Stolen, J. P. Gordon, W. J. Tomlinson, and H. A. Haus, "Raman response function of silica-core fibers," *J. Opt. Soc. Am. B*, vol. 6, no. 6, pp. 1159–1166, 1989.

[51] R. Shuker and R. W. Gammon, "Raman-scattering selection-rule breaking and the density of states in amorphous materials," *Phys. Rev. Lett.*, vol. 25, pp. 222–225, 1970.

[52] S. Coen, A. H. L. Chau, R. Leonhardt, J. D. Harvey, J. C. Knight, W. J. Wadsworth, and P. S. J. Russell, "Supercontinuum generation by stimulated raman scattering and parametric four-wave mixing in photonic crystal fibers," *J. Opt. Soc. Am. B*, vol. 19, no. 4, pp. 753–764, 2002.

[53] N. Bloembergen and Y. Shen, "Coupling between vibrations and light waves in raman laser media," *Phys. Rev. Lett.*, vol. 12, pp. 504–507, 1964.

[54] P. Beaud, W. Hodel, B. Zysset, and H. Weber, "Ultrashort pulse propagation, pulse breakup, and fundamental soliton formation in a single-mode optical fiber," *Quantum Electronics, IEEE Journal of*, vol. 23, no. 11, pp. 1938–1946, 1987.

[55] D. Peregrine, "Water waves, nonlinear schrödinger equations and their solutions," *J. Austr. Math. Soc.*, vol. 25, no. 1, pp. 16–43, 1983.

[56] C. Sulem, *The Nonlinear Schrödinger Equation: Self-Focusing and Wave Collapse*, 1st ed. Springer, 1999.

[57] K. Blow and D. Wood, "Theoretical description of transient stimulated raman scattering in optical fibers," *Quantum Electronics, IEEE Journal of*, vol. 25, no. 12, pp. 2665–2673, 1989.

[58] A. Antikainen, "Higher-order correlations of supercontinuum light," Master of Science thesis, Tampere University of Technology, 2013.

[59] C. Lin and R. Stolen, "New nanosecond continuum for excited-state spectroscopy," *Appl. Phys. Lett.*, vol. 28, pp. 216–218, 1976.

[60] R. F. Cregan, B. J. Mangan, J. C. Knight, T. A. Birks, P. S. J. Russell, P. J. Roberts, and D. C. Allan, "Single-mode photonic band gap guidance of light in air," *Science*, vol. 285, no. 5433, pp. 1537–1539, 1999.

[61] K. Shi, P. Li, S. Yin, and Z. Liu, "Chromatic confocal microscopy using supercontinuum light," *Opt. Express*, vol. 12, no. 10, pp. 2096–2101, 2004.

[62] R. Wu, V. Torres-Company, D. E. Leaird, and A. M. Weiner, "Supercontinuum-based 10-ghz flat-topped optical frequency comb generation," *Opt. Express*, vol. 21, no. 5, pp. 6045–6052, 2013.

[63] T. Morioka, H. Takara, S. Kawanishi, O. Kamatani, K. Takiguchi, K. Uchiyama, M. Saruwatari, H. Takahashi, M. Yamada, T. Kanamori, and H. Ono, "1 tbit/s (100 gbit/s times;10 channel) otdm/wdm transmission using a single supercontinuum wdm source," *Electronics Letters*, vol. 32, no. 10, pp. 906–907, 1996.

[64] L. Mandel and E. Wolf, *Optical Coherence and Quantum Optics*, 1st ed. Cambridge University Press, 1995.

[65] E. Wolf, "New theory of partial coherence in the space-frequency domain. part i: spectra and cross spectra of steady-state sources," *J. Opt. Soc. Am.*, vol. 72, no. 3, pp. 343–351, 1982.

[66] M. Erkintalo, M. Surakka, J. Turunen, A. T. Friberg, and G. Genty, "Coherent-mode representation of supercontinuum," *Opt. Lett.*, vol. 37, no. 2, pp. 169–171, 2012.

[67] P. Vahimaa and J. Turunen, "Independent-elementary-pulse representation for non-stationary fields," *Opt. Express*, vol. 14, no. 12, pp. 5007–5012, 2006.

[68] M. Korhonen, A. T. Friberg, J. Turunen, and G. Genty, "Elementary field representation of supercontinuum," *J. Opt. Soc. Am. B*, vol. 30, no. 1, pp. 21–26, 2013.

[69] C. Lawson and R. Hanson, *Solving Least Squares Problems*, 1st ed. Prentice-Hall, 1974.

[70] R. Trebino, K. W. DeLong, D. N. Fittinghoff, J. N. Sweetser, M. A. Krumbugel, B. A. Richman, and D. J. Kane, "Measuring ultrashort laser pulses in the time-frequency domain using frequency-resolved optical gating," *Review of Scientific Instruments*, vol. 68, no. 9, pp. 3277–3295, 1997.

[71] J. R. Fienup, "Phase retrieval algorithms: a personal tour," *Appl. Opt.*, vol. 52, no. 1, pp. 45–56, 2013.

[72] E. Akutowicz, "On the determination of the phase of a fourier integral, i and ii," *Trans. Amer. Math. Soc.*, vol. 84, pp. 234–238, 1957.

[73] R. Gerchberg and W. Saxton, "A practical algorithm for the determination of phase from image and diffraction plane pictures," *Optik*, vol. 35, no. 2, pp. 237–246, 1971.

[74] D. Kane and R. Trebino, "Characterization of arbitrary femtosecond pulses using frequency-resolved optical gating," *Quantum Electronics, IEEE Journal of*, vol. 29, no. 2, pp. 571–579, 1993.

[75] K. W. DeLong and R. Trebino, "Improved ultrashort pulse-retrieval algorithm for frequency-resolved optical gating," *J. Opt. Soc. Am. A*, vol. 11, no. 9, pp. 2429–2437, 1994.

[76] J. R. Fienup, "Phase retrieval algorithms: a comparison," *Appl. Opt.*, vol. 21, no. 15, pp. 2758–2769, 1982.

[77] P. O'Shea, M. Kimmel, X. Gu, and R. Trebino, "Increased-bandwidth in ultrashort-pulse measurement using an angle-dithered nonlinear-optical crystal," *Opt. Express*, vol. 7, no. 10, pp. 342–349, 2000.

[78] K. DeLong, D. Fittinghoff, and R. Trebino, "Practical issues in ultrashort-laser-pulse measurement using frequency-resolved optical gating," *Quantum Electronics, IEEE Journal of*, vol. 32, no. 7, pp. 1253–1264, 1996.